



Contents lists available at ScienceDirect

## International Journal of Solids and Structures

journal homepage: [www.elsevier.com/locate/ijsolstr](http://www.elsevier.com/locate/ijsolstr)

# Influence of rock heterogeneity on hydraulic fracturing: A parametric study using the combined finite-discrete element method

Mingyang Wu<sup>a,b</sup>, Ke Gao<sup>b,\*</sup>, Jianjun Liu<sup>c</sup>, Zhenlong Song<sup>b</sup>, Xiaolin Huang<sup>d,\*</sup>

<sup>a</sup> State Key Laboratory of Coal Mine Disaster Dynamics and Control, School of Resources and Safety Engineering, Chongqing University, Chongqing 400030, China

<sup>b</sup> Department of Earth and Space Sciences, Southern University of Science and Technology, Shenzhen 518055, China

<sup>c</sup> State Key Laboratory of Geomechanics and Geotechnical Engineering, Wuhan Institute of Rock and Soil Mechanics, Chinese Academy of Science, Wuhan 430071, China

<sup>d</sup> Key Laboratory of Shale Gas and Geoenvironment, Institute of Geology and Geophysics, Chinese Academy of Sciences, Beijing 100029, China

## ARTICLE INFO

## Keywords:

Hydraulic fracturing  
Combined finite-discrete element method  
Rock heterogeneity  
Propagation regimes  
Fracture morphology

## ABSTRACT

Hydraulic fracturing has proven to be an efficient technique to enhance production in unconventional reservoirs. Since heterogeneity is commonplace in reservoir rocks, it is vital to investigate the influence of rock heterogeneity on hydraulic fracture propagation. Here, based on the combined finite-discrete element method (FDEM) and cohesive zone model, two series of numerical models with uniformly distributed and Weibull-distributed elastic modulus of rock are assembled, respectively. The comparison with the theoretical solution demonstrates the reliability of the simulation models in both the toughness-dominated regime (TDR) and viscosity-dominated regime (VDR). The parameter analysis demonstrates the rationality of parameters for cohesive elements. The results show that the previous theoretical equations can be used as a preliminary evaluation of simulation parameters. The effects of different parameters such as element size, Weibull distribution type, and far-field stress on hydraulic fracture length, fluid pressure, maximum fracture aperture, and the final fracture morphology are evaluated. The results demonstrate that the distribution type of rock elastic modulus has a significant impact on the hydraulic fracture propagation in both TDR and VDR. The “jump” phenomena have been observed in TDR caused by high fracture toughness. The displacement of fracture location and asymmetrically dynamic propagation are affected by the distribution of rock elastic modulus. Besides, the hydraulic fracture propagation in TDR is more susceptible to element size, the distribution of rock elastic modulus, and far-field stress than that in VDR. This research may shed light on the development of hydraulic fracturing technology in tight reservoirs.

## 1. Introduction

Hydraulic fracturing technique has been widely used to increase the permeability of tight reservoir rocks, with the ultimate goal of enhancing oil and gas production in unconventional reservoirs (Carrier and Granet, 2012; Detournay, 2016; Wang, 2019; Wu et al., 2020). However, material heterogeneity is commonplace in reservoir rocks (Ju et al., 2016; Lei and Gao, 2019; Liu et al., 2018; Ma et al., 2018; Valiappan et al., 2017), and it may have great impacts on the propagation of hydraulic fractures. Therefore, it is necessary to investigate the influence of rock heterogeneity on hydraulic fracturing.

Previously, average values of mechanical parameters of rock samples obtained at mesoscopic scale are commonly used as the equivalent mechanical parameters of oil and gas reservoir at macro scale (as shown

in Fig. 1). In fact, after many years sedimentation and diagenesis, oil and gas reservoirs usually have different degrees of heterogeneities (Doughty et al., 1994). However, due to the difficulty of implementation and the limitation of monitoring tools, it is difficult to study the heterogeneity and its effect on hydraulic fracturing in laboratory experiments (Deng et al., 2018b; Wu et al., 2020). Thus, numerical models considering rock heterogeneity characteristics have to be established for such study.

As a matter of fact, hydraulic fracture propagation has been numerically studied by many researchers (e.g., Cheng et al., 2017; Dahi Taleghani et al., 2018; Dahi Taleghani et al., 2016; Huang et al., 2019; Ju et al., 2016; Salimzadeh and Khalili, 2015; Salimzadeh et al., 2017; Wu et al., 2018; Yan et al., 2016; Zhang and Dontsov, 2018; Zhang et al., 2017). Finite element method (FEM), due to its versatility and maturity,

\* Corresponding authors.

E-mail addresses: [gaok@sustech.edu.cn](mailto:gaok@sustech.edu.cn) (K. Gao), [huangxiaolin@mail.iggcas.ac.cn](mailto:huangxiaolin@mail.iggcas.ac.cn) (X. Huang).

<https://doi.org/10.1016/j.ijsolstr.2021.111293>

Received 12 May 2021; Received in revised form 6 September 2021; Accepted 8 October 2021

Available online 16 October 2021

0020-7683/© 2021 Elsevier Ltd. All rights reserved.

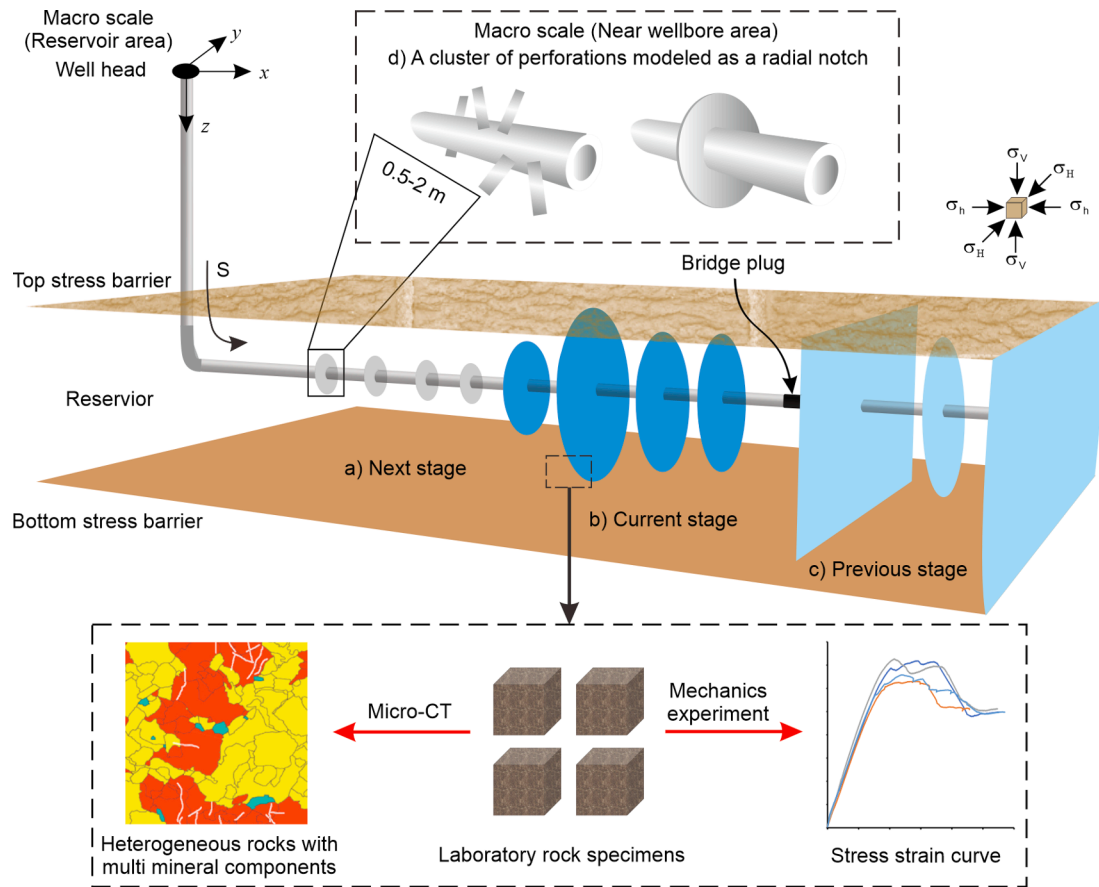


Fig. 1. Sketch of hydraulic fracturing operation and laboratory test results of reservoir parameters. (Modified from Lecampion and Desroches (2015) and Zhuang et al. (2020)).

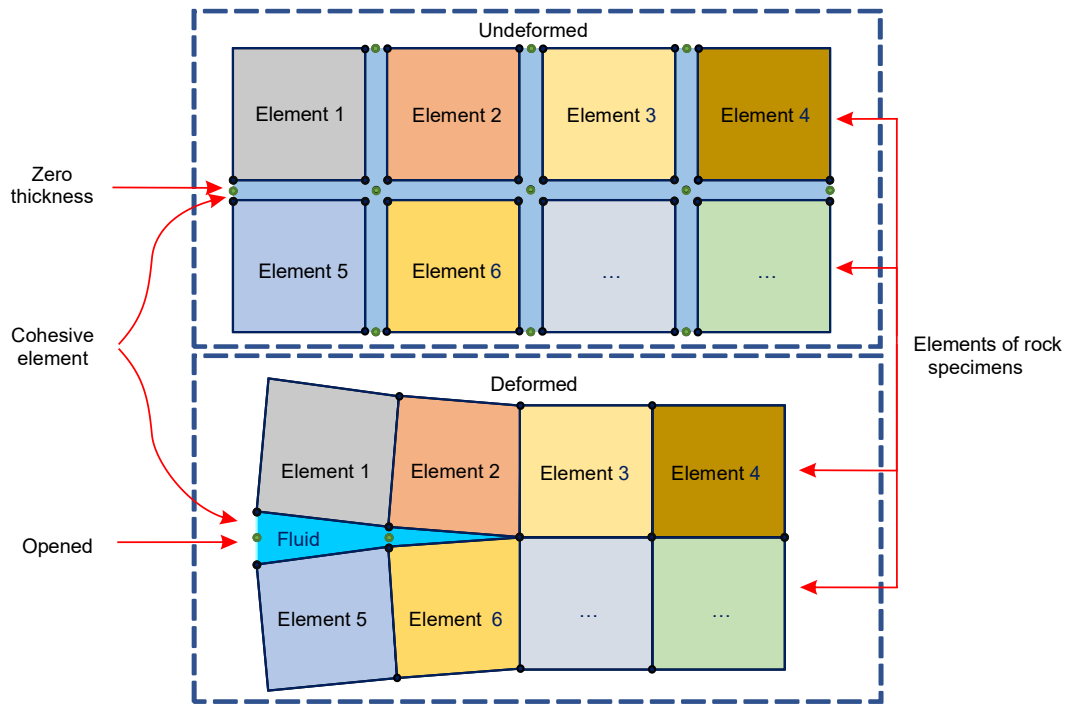


Fig. 2. Demonstration of elements in a heterogeneous FDEM model used in the present paper.

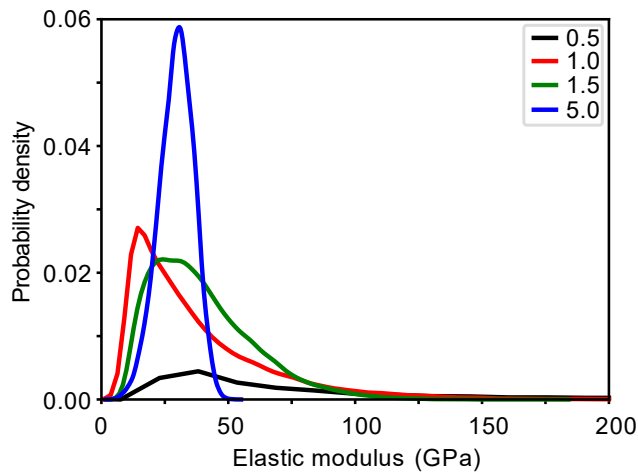


Fig. 3. Variability of elastic modulus in a rock specimen characterized by different Weibull distribution types.

Table 1

Main parameters used in the theoretical solutions for VDR and TDR.

Parameters	VDR	TDR
$\bar{E}_b$ (GPa)	29.5	29.5
$\nu$	0.292	0.292
$Q_0$ (m <sup>2</sup> /s)	$1 \times 10^{-4}$	$3 \times 10^{-7}$
$t$ (s)	0.1	9.0
$u$ (cp)	100	2
$K_m$	0.653	16.4
$\sigma_H/\sigma_h$ (MPa)	15/10	15/10

is among one of the most commonly used, especially in the early practice of hydraulic fracturing simulation (Adachi et al., 2007; Carrier and Granet, 2012). In FEM models, reservoir rocks are often considered as continuous media, and thus uniform parameter values are assigned to all numerical elements. As an improvement, Ju et al. (2016) divided the rock specimen into matrix and gravels using the continuum-based discrete element method (CDEM), and different mechanical parameters were assigned to the elements according to their physical association. In their models, the rock heterogeneity is weighed by gravel volumetric fraction, so the effect of rock heterogeneity on hydrofracturing behavior of a heterogeneous rock has been analyzed. The simulation results show that the rock heterogeneity has considerable

effect on crack initiation, which indicates the necessity of heterogeneous model for understanding hydraulic fracture propagation. Following this, few other heterogeneous models have been found to further study the influence of rock heterogeneity on hydraulic fracturing (e.g., Wang, 2019; Wu et al., 2019).

In recent years, theoretical researches demonstrate that hydraulic fractures have many propagation regimes, e.g., the toughness-dominated regime (TDR) and viscosity-dominated regime (VDR) (Detournay, 2016; Dontsov, 2017). Unfortunately, this has not been considered in the previous heterogeneity studies. Therefore, it is necessary to investigate the influence of different hydraulic fracture propagation regimes in the rock heterogeneity analysis. As an example of such implementation, Huang et al. (2019) presented both homogeneous and heterogeneous models using particle-based discrete element method (DEM), and the effects of rock inherent heterogeneity and grain size on hydraulic fracture initiation and propagation in both TDR and VDR are discussed. Their simulation results are helpful to understand hydraulic fracture propagation in heterogeneous rocks under different propagation regimes. However, due to the nature of particle flow DEM, the variability of key parameters such as fracture aperture cannot be precisely acquired. Additionally, considering that the rock heterogeneity in the particle-based DEM is realized by rigid particle distributions, which seems different from our general understanding of rock material heterogeneity, alternative approaches such as the combined finite-discrete element method (FDEM) (Lei and Gao, 2018, 2019; Munjiza, 2004) should be employed to further explore this. The FDEM, due to its capability to explicitly represent rock heterogeneity and dynamically simulate the progressive evolution of fracture morphology, provides a useful tool to thoroughly investigate hydraulic fracture propagation under different propagation regimes and rock heterogeneity characteristics.

In this paper, both homogenous and heterogeneous models under different hydraulic fracture control regimes are established using FDEM and the difference between them is compared. The influences of element size, distribution type of rock elastic modulus and far-field stress on the variation of breakdown pressure, propagation pressure, fracture length, and maximum fracture aperture in different models and control regimes are analyzed. The corresponding theories are introduced in Sections 2, followed by the model calibration with theoretical solutions in Sections 3. The results are depicted in Sections 4 and the conclusions are given at the end.

## 2. Theories in a nutshell

To give a clear demonstration of the methods used in the present

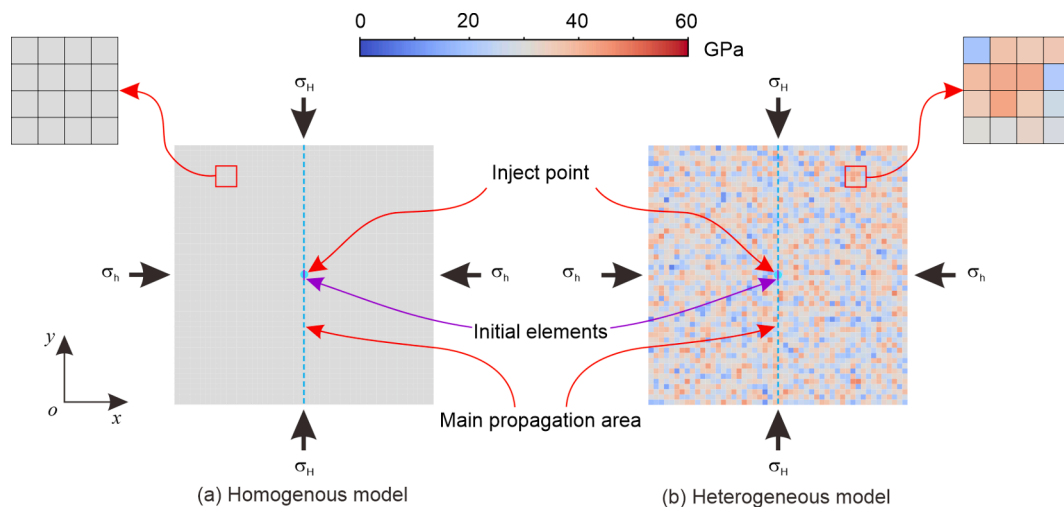


Fig. 4. Schematic of the hydraulic fracturing model, (a) homogenous model, and (b) heterogeneous model (the color represents the value of rock elastic modulus).

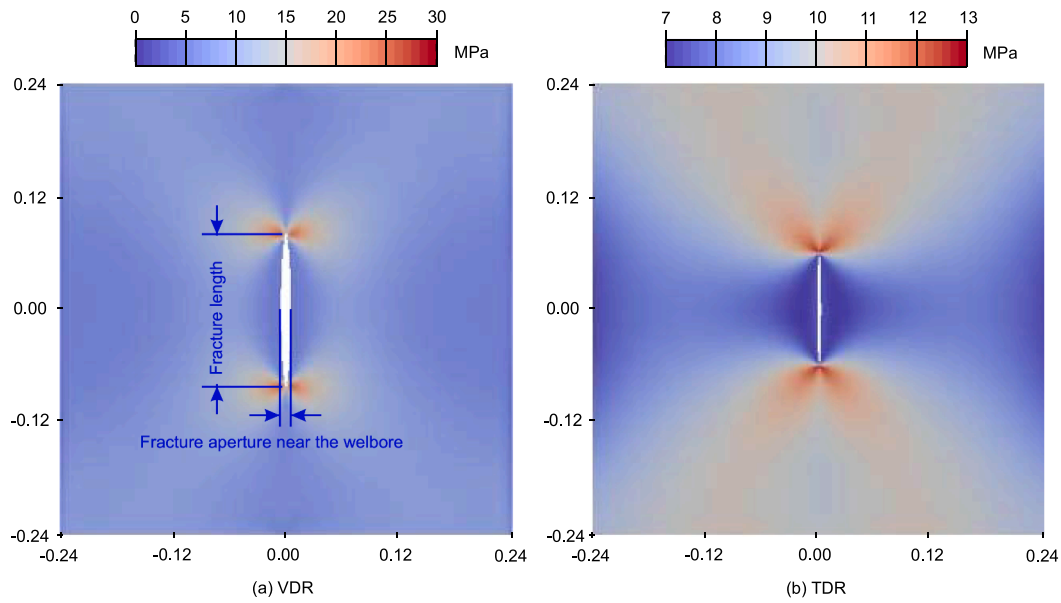


Fig. 5. Final stress nephogram of simulated (homogeneous) models in (a) VDR (0.1 s) and (b) TDR (9 s).

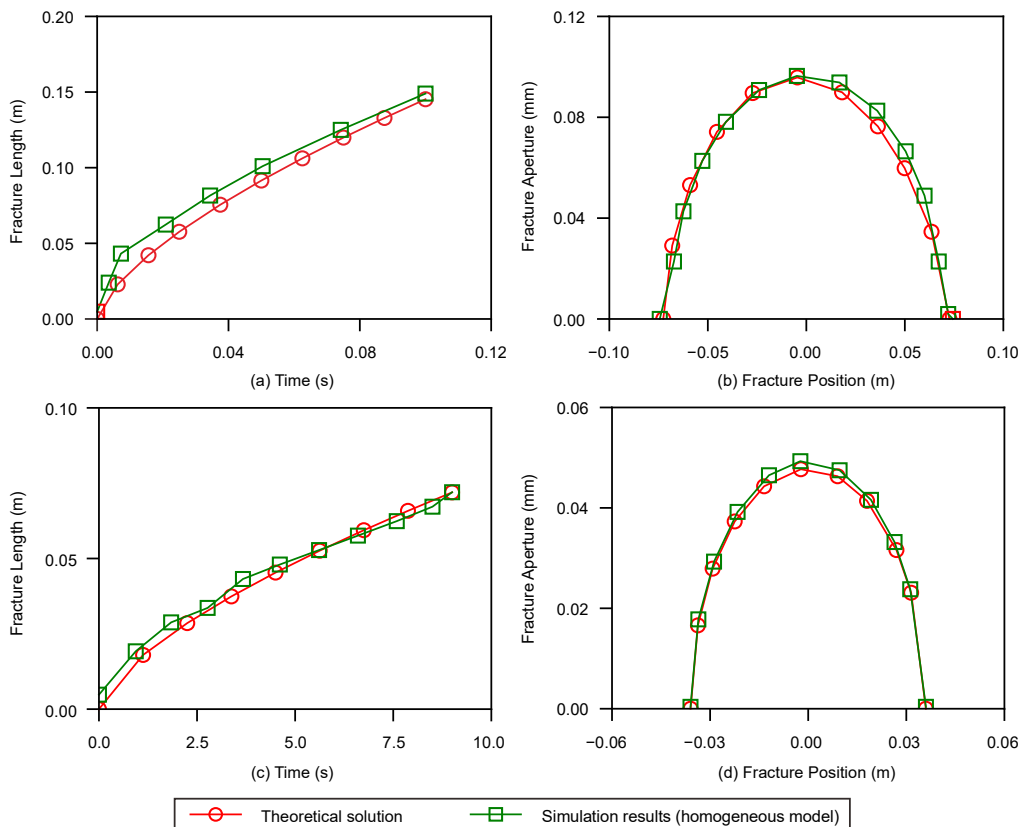
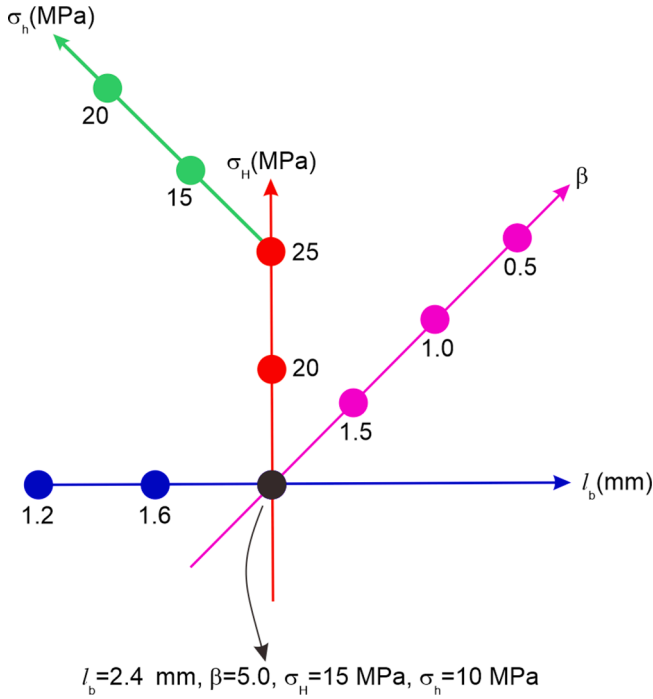


Fig. 6. Comparison between the theoretical solution and simulation results (homogeneous model) in VDR (top row, i.e., a & b) and TDR (bottom row, i.e., c & d) in terms of hydraulic fracture length versus injection time (left column, i.e., a & c) and the fracture aperture versus fracture position (right column, i.e., b & d).

study, in this section, we first present an overview of the theories of FDEM. This is followed by the illustration of the theory and implementation of cohesive element used for hydraulic fracturing simulation. In addition, a detailed demonstration of the heterogeneous model using the Weibull distribution of rock elastic modulus is elucidated in Section 2.3.

### 2.1. Overview of FDEM

FDEM was pioneered by Dr. Munjiza (Munjiza, 2004) and has been significantly improved after many years developments (Knight et al., 2020; Lei et al., 2014; Lisjak et al., 2013; Xiang et al., 2009a; Xiang et al., 2009b; Yan et al., 2018). In previous applications, FDEM has proven to be an effective and reliable tool for solving rock mechanics related



**Fig. 7.** Illustration of the four groups of models for examining the influence of element size  $l_b$  (blue), shape parameter  $\beta$  (magenta), maximum far-field stress  $\sigma_H$  (red), and minimum far-field stress  $\sigma_h$  (green) on hydraulic fracture propagation. (For interpretation of the references to color in this figure legend, the reader is referred to the web version of this article.)

problems, e.g., stress analysis, stress effects on rock mass permeability and rock fracture behavior (Latham et al., 2013; Lei and Gao, 2018, 2019; Lei et al., 2019; Rougier et al., 2020). Compared with traditional DEM, FDEM can meet the requirements of simulating rock mechanical behaviors from laboratory samples to reservoir scales. The FDEM represents a rock model using a full mesh of finite elements, and adjacent elements are further linked by cohesive element. When loads are applied to the rock, the motions of finite elements can be calculated by the forces acting on elemental nodes; the deformation of finite elements can be calculated by the corresponding constitutive relations. The cohesive elements embedded in the FDEM formulation further permits the simulator to capture the initiation and propagation of fractures.

Based on FDEM, heterogeneous rock specimens are assumed to be composed of rock elements and zero-thickness cohesive elements (Fig. 2). With continuous fluid injection, hydraulic fractures can be formed between rock elements. Therefore, when the boundary and load conditions are determined, the hydraulic fracturing process of reservoir rock specimen can be readily simulated. The fluid–solid coupling process and the solution of time step during fracturing is solved by the corresponding coupling governing equations (Dahi Taleghani et al., 2018; Dahi Taleghani et al., 2016; Guo et al., 2015; Wu et al., 2020; Wu et al., 2018). For clarity, details regarding the fluid–solid coupling procedure are illustrated in Appendix A.

## 2.2. Cohesive zone model

At the onset of simulation, adjacent rock elements are connected by zero-thickness global cohesive elements, with the purpose to dynamically simulate hydraulic fracture propagation. The behavior of cohesive elements is controlled by a traction–separation law. Before damage occurs, the stress and strain of the cohesive element satisfy the linear elastic relationship (Guo et al., 2015; Wu et al., 2020)

$$\sigma_{\text{coh}} = \begin{bmatrix} \sigma_{\text{cohn}} \\ \sigma_{\text{cohs}} \end{bmatrix} = \mathbf{K}_{\text{coh}} \boldsymbol{\varepsilon}_{\text{coh}} = \begin{bmatrix} K_{\text{cohn}} & K_{\text{cohns}} \\ K_{\text{cohs}} & K_{\text{cohss}} \end{bmatrix} \begin{bmatrix} \varepsilon_{\text{cohn}} \\ \varepsilon_{\text{cohs}} \end{bmatrix} \quad (1)$$

where  $\sigma_{\text{coh}}$  denotes the stress in a cohesive element, and  $\sigma_{\text{cohn}}$  and  $\sigma_{\text{cohs}}$  are the normal and tangential stress, respectively;  $\mathbf{K}_{\text{coh}}$  denotes the stiffness matrix of a cohesive element;  $\boldsymbol{\varepsilon}_{\text{coh}}$  is the strain matrix of a cohesive element, and  $\varepsilon_{\text{cohn}}$  and  $\varepsilon_{\text{cohs}}$  represent respectively the normal and tangential strain, i.e.,

$$\varepsilon_{\text{cohn}} = \frac{d_n}{T_0}, \quad \varepsilon_{\text{cohs}} = \frac{d_s}{T_0} \quad (2)$$

here  $d_n$  and  $d_s$  represent the normal and tangential displacement of a cohesive element, respectively, and  $T_0$  is the constitutive thickness of the cohesive element.

The initiation of hydraulic fractures is controlled by the damage criterion of cohesive element. The maximum stress criterion adopted was

$$\left\{ \frac{\langle \sigma_n \rangle}{\sigma_n^0} \right\}^2 + \left\{ \frac{\sigma_s}{\sigma_s^0} \right\}^2 = \lambda$$

where  $\sigma_n$  and  $\sigma_s$  are the normal and tangential stresses respectively,  $\sigma_n^0$  and  $\sigma_s^0$  are the threshold stresses of normal and tangential damage,  $\langle \cdot \rangle$  indicates that cohesive elements resist tension stress only, and  $1 \leq \lambda \leq 1.05$ . A linear degradation criterion is used to describe the attenuation of elastic modulus of a cohesive element after damage (Dahi Taleghani et al., 2016)

$$E_{\text{coh}} = (1 - d) E_{\text{coh}}^0 \quad (4)$$

where  $E_{\text{coh}}^0$  and  $E_{\text{coh}}$  are the initial elastic modulus of cohesive element (without damage) and the elastic modulus after damage, respectively. Here,  $d$  denotes the stiffness degradation variable (SDEG), i.e., the damage factor, which can be calculated by (Dahi Taleghani et al., 2018)

$$d = \frac{\delta_m^f (\delta_m^{\text{max}} - \delta_m^0)}{\delta_m^{\text{max}} (\delta_m^f - \delta_m^0)}$$

where  $\delta_m^{\text{max}}$ ,  $\delta_m^0$  and  $\delta_m^f$  respectively represent the maximum displacement of the cohesive element during loading, the displacement when the element is initially damaged, and the displacement when the element is completely damaged.

Similar to the theoretical solution and the previous DEM simulation (Dontsov, 2017; Huang et al., 2019), only tangential flow along the cohesive elements is simulated in this paper. For a tangential flow, the fluid is assumed to be an incompressible Newtonian fluid. The volume flow per element length along the tangential direction is given by

$$q = \frac{w^3}{12\mu} \nabla p \quad (6)$$

where  $w$  is the thickness of cohesive element,  $\mu$  is the viscous coefficient of fluid, and  $p$  is the fluid pressure in a cohesive element.

## 2.3. Weibull distribution of rock elastic modulus

Weibull distribution of rock elastic modulus is widely used to describe the heterogeneity of rock masses (Lei and Gao, 2018, 2019; Li et al., 2020; Yang et al., 2009), and is thus employed here to realize heterogeneous rock models. Assuming that the elastic modulus of various rock specimens from a reservoir is  $E_b$ , the elastic modulus of rock in a homogeneous model can be approximated by its mean value  $\bar{E}_b$ . When the distribution characteristics of rock elastic modulus is considered, its probability density function following Weibull distribution is described by (Lei and Gao, 2018, 2019; Li et al., 2020; Yang et al., 2009)

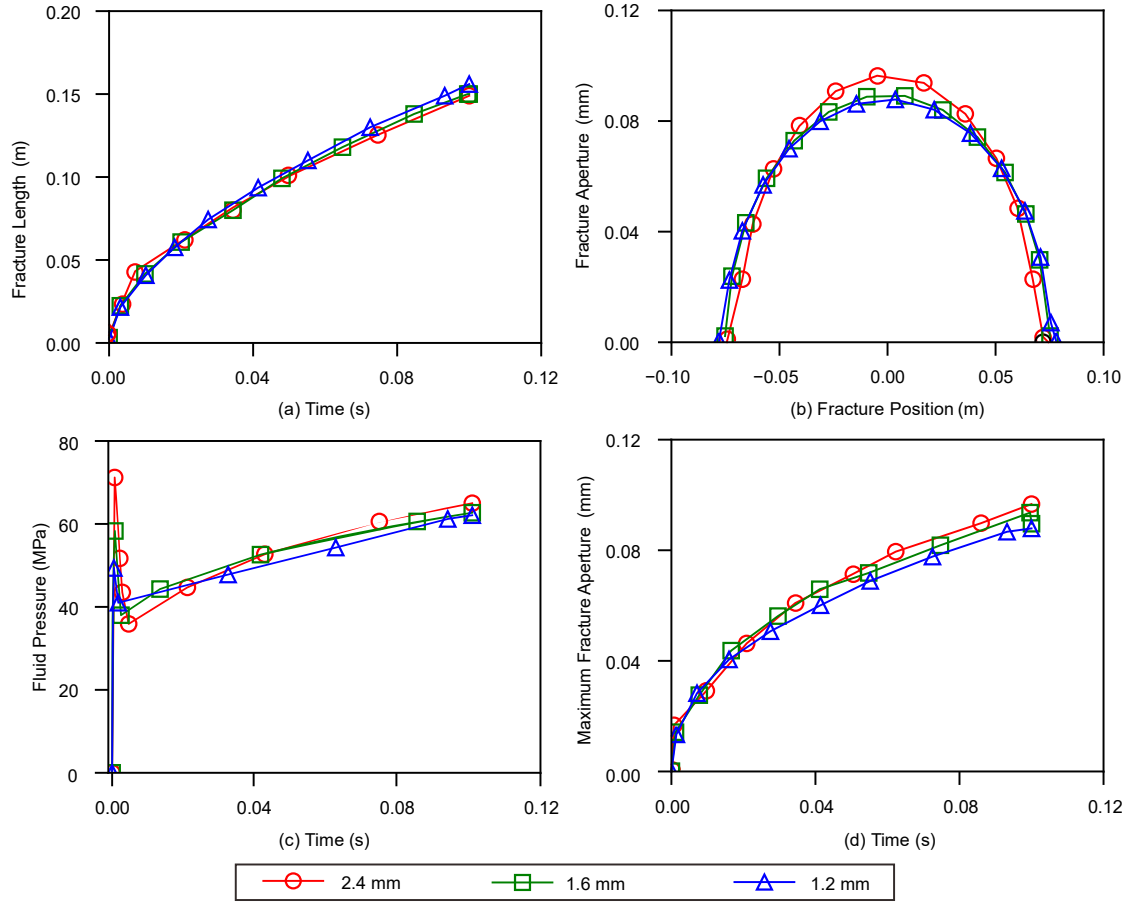


**Fig. 8.** Simulation results of hydraulic fracturing in VDR for the three homogeneous models using different element sizes in terms of (a) fracture length versus injection time, (b) fracture aperture versus fracture position, (c) fluid pressure versus injection time, and (d) maximum fracture aperture versus injection time.

$$f(E_b; \beta) = \frac{\beta}{E_b} \left( \frac{E_b}{E_0} \right)^{\beta-1} \exp \left[ - \left( \frac{E_b}{E_0} \right)^\beta \right] \quad (7)$$

where  $\beta$  ( $\beta > 0$ ) is a shape parameter or material homogeneity index, and different  $\beta$  will result in different probability density curves. For example, when  $\beta = 1$ , it is an exponential distribution; when  $\beta = 2$ , it becomes a Rayleigh distribution. Generally, the smaller  $\beta$  is, the more heterogeneous the rock would be. Referring to the previous research (Lei and Gao, 2019), typical distribution functions of rock elastic modulus for  $\beta$  of 0.5, 1.0, 1.5, and 5.0 are selected in the present paper, which cover the conditions from highly heterogeneous to relatively homogeneous. The corresponding curves are plotted in Fig. 3. It is manifest that under these four types of Weibull distribution, their ranges of minimum values of rock elastic modulus are relatively close, while the maximum values could vary. With the increase of  $\beta$ , the maximum values of rock elastic modulus gradually decrease, while the probability of small elastic modulus gradually increases. This may mean that with the increase of  $\beta$ , the proportion of stiff rock blocks (large elastic modulus) decreases significantly. We realize the heterogeneous rock models by first generating a series of random numbers following a specific Weibull distribution based on the number of elements meshed for a rock model, and then assign these values to each element accordingly.

### 3. Numerical model calibration

Before investigating the influence of heterogeneity on hydraulic fracturing, we first calibrate our FDEM models with the theoretical solutions. This starts with a presentation of the theoretical solutions of the two control regimes we are going to compare with. Then, the details of

the model are introduced, and the parameters adopted in the simulation are analyzed to demonstrate the rationality of our models. The comparison between the analytical solution and simulation results is shown at the end.

#### 3.1. Theoretical solutions

The main theoretical solution related to hydraulic fracture propagation can be originated to the Khristianovich–Geertsma–DeKlerk (KGD) model, which was first developed by Zheltov (1955) and Geertsma and De Klerk (1969). After extensive derivation, theoretical solutions under VDR and TDR (without fluid leak-off) are obtained by Dontsov (2017) and Zhang and Dontsov (2018), which overcome the limitations of the early theoretical solution. The basic material parameters in the theoretical solution are

$$u' = 12u \quad (8)$$

$$E' = \frac{E}{1 - \nu^2} \quad (9)$$

$$K' = 4\sqrt{\frac{2}{\pi}} K_{IC} \quad (10)$$

and

$$C' = 2C_L \quad (11)$$

where  $u$  is the Newtonian fluid viscosity,  $E$  is the rock elastic modulus,  $\nu$  is the Poisson's ratio,  $K_{IC}$  is the mode I fracture toughness of the rock,

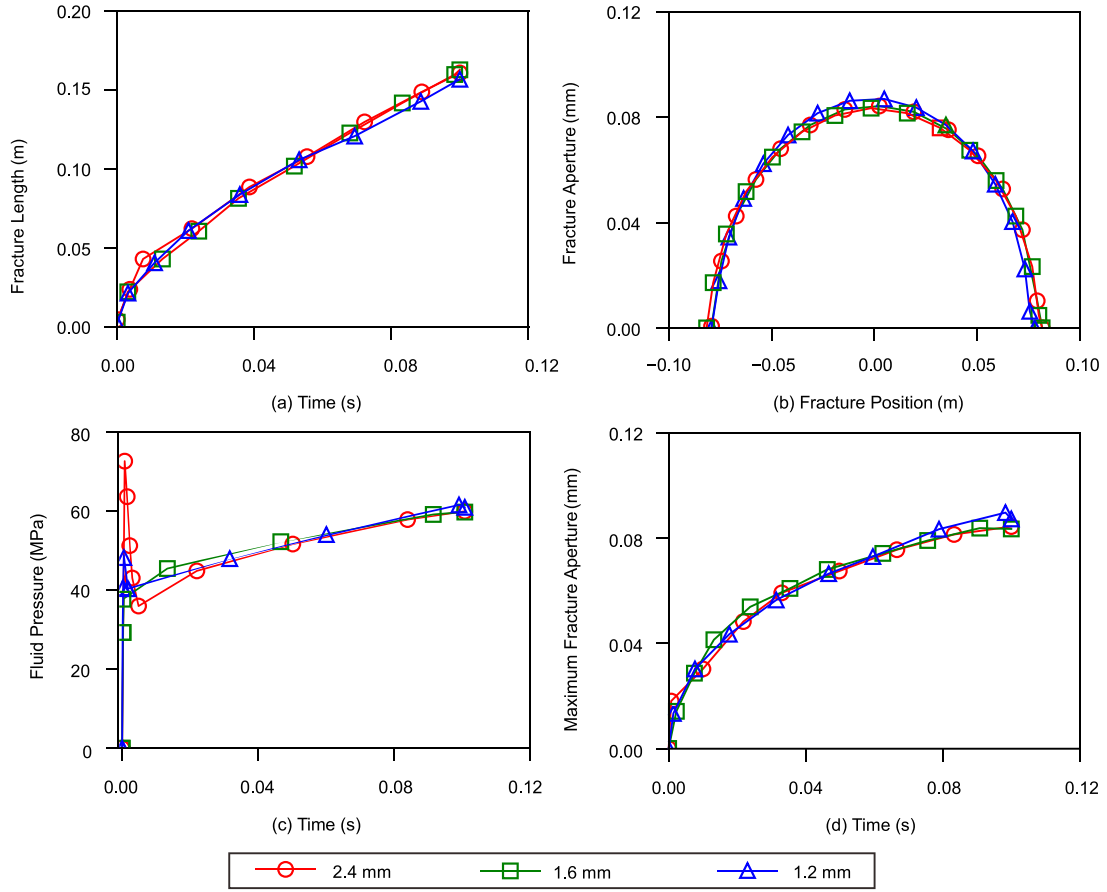


Fig. 9. Simulation results of hydraulic fracturing in VDR for the three heterogeneous models using different element sizes in terms of (a) fracture length versus injection time, (b) fracture aperture versus fracture position, (c) fluid pressure versus injection time, and (d) maximum fracture aperture versus injection time.

and  $C_L$  is the Carter's leak-off parameter (Nolte, 1986).

In VDR, the fluid viscosity is the main factor affecting hydraulic fracture propagation (Dontsov, 2017); while in TDR, the rock fracture toughness becomes the main factor. Different control mechanisms are directly determined by the dimensionless time and the toughness parameter (Dontsov, 2017; Huang et al., 2019). The fracture aperture and fracture half-length evolution with respect to time in the theoretical solution of VDR can be respectively expressed as (Zhang and Dontsov, 2018; Zhang et al., 2017)

$$w_m(\xi, t) = 1.1265 \left( \frac{u' Q_0^3 t^2}{E} \right)^{1/6} (1 + \xi)^{0.588} (1 - \xi)^{2/3} \quad (12)$$

and

$$l_m(t) = 0.6159 \left( \frac{Q_0^3 E t^4}{u'} \right)^{1/6} \quad (13)$$

where  $\xi$  ( $\xi = x/l$ ) is the normalized coordinate along the fracture ( $x$  is the distance measured from the injection point,  $l$  is the fracture half-length). The subscript  $m$  represents the VDR,  $t$  denotes injection time, and  $Q_0$  is injection rate. The fracture aperture and fracture half-length evolution with respect to time in the theoretical solution of TDR can be respectively expressed as (Dontsov, 2017)

$$w_k(\xi, t) = 0.6828 \left( \frac{(K')^2 Q_0 t}{(E')^2} \right)^{1/3} (1 - \xi^2)^{1/2} \quad (14)$$

and

$$l_k(t) = 0.9324 \left( \frac{E' Q_0 t}{K'} \right)^{2/3} \quad (15)$$

where the subscript  $k$  represents the TDR.

The reasonable selection of parameters is key to the rationality of modeling results. In addition to the calibration with the theoretical solutions, we have also checked our simulation results with the existing researches. To facilitate comparison with the previous similar research conducted using DEM (Huang et al., 2019), the mean rock elastic modulus, Poisson's ratio, and far-field stress for the VDR and TDR are chosen to be the same, as are tabulated in Table 1. Additionally, our tests indicate that the rock fracture toughness in TDR used in the previous study is relatively small, so here a properly enlarged fracture toughness is used in the theoretical solution in TDR. Details of the fracture toughness selection in TDR is explained in Appendix B.

### 3.2. Model setup

The FDEM rock model used in the present analysis is of square shape with an edge length of 0.48 m, which is same as the one used in the previous DEM simulation (Huang et al., 2019). In our previous study (Wu et al., 2021), the differences between structured (symmetric) and unstructured (asymmetric) grids have been discussed. The results show that the hydraulic fractures under unstructured grid tend to be curved, while the hydraulic fractures under the influence of structured grid are mainly linear. Additionally, pure mode I fracture is generally assumed in the analytical solution model (Detournay, 2004; Dontsov, 2017; Dontsov and Peirce, 2015, 2016; Dontsov and Suarez-Rivera, 2020). To make the fracture mode of the simulation results closer to the analytical

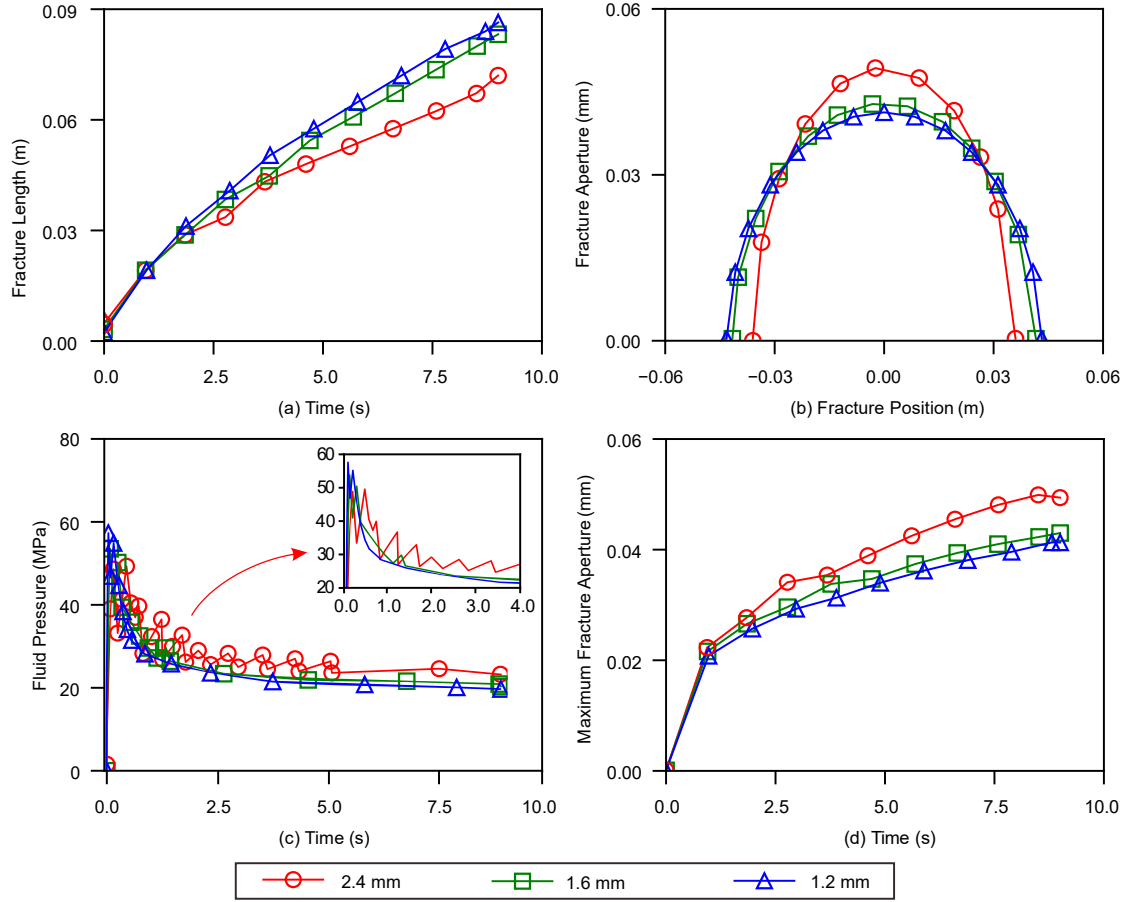


Fig. 10. Simulation results of hydraulic fracturing in TDR for the three homogeneous models of different element size in terms of (a) fracture length versus injection time, (b) fracture aperture versus fracture position, (c) fluid pressure versus injection time, and (d) maximum fracture aperture versus injection time.

solution and to design a strict control group based on homogeneous model, structured quadrilateral elements, i.e., symmetric grids, are used here to mesh the rock specimen. A total of 40,000 elements are generated for the model with an element size of 2.4 mm.

A series of rock elastic modulus values with specific distribution characteristics and their average value are used to establish the heterogeneous and homogeneous models, respectively. Under this condition, when  $\beta = 5$  and the average elastic modulus is 29.5 GPa, the elastic modulus obtained by Eq. (7) is mainly distributed in the range of 0–60 GPa. For demonstration purpose, a rock specimen consists of 10,000 elements is shown in Fig. 4. The maximum far-field stress  $\sigma_H$  is acting vertically and the minimum far-field stress  $\sigma_h$  horizontally on the model edges. The injection point is placed at the center of the sample and two initially damaged cohesive elements near the injection point are created to facilitate model convergence. The basic simulation parameters in the simulation models are presented in Table 1. Please note that due to the differences between the theoretical solution, DEM, and FDEM, additional parameters have been set to make our models closer to reality. These additional parameters of rock elements were set according to previous studies. For example, the hydraulic fracturing reservoirs are usually with low porosity and low permeability (Dahi Taleghani et al., 2018; Dahi Taleghani et al., 2016; Guo et al., 2015; Wu et al., 2020; Wu et al., 2018), thus the initial void ratio of rock is set to 0.001, and 1 mD is taken as the permeability value. The gravity of water is set to 9,800 N/m<sup>3</sup>. In addition, it is known that the main challenge in using cohesive models lies in the appropriate selection of cohesive element parameters from experiments or theories (Dahi Taleghani et al., 2016). Therefore, extra theoretical formulas are used to verify the reliability of the additional parameters of cohesive elements chosen in the present paper, as is

demonstrated next.

In the analytical solution, pure mode I fracture is assumed. When the mode I fracture toughness of a rock specimen has been replaced by the constitutive parameters of cohesive element, the fracture energy of cohesive element can be calculated by (Schwalbe et al., 2013)

$$G_c = \int_0^{\delta_m} T(\delta) d\delta \quad (16)$$

where  $G_c$  is within a range of 10–10,000 N/m,  $T$  is the traction, and  $\delta$  is the separation. In this paper,  $G_c$  of bilinear or triangular law can be simplified to (Dahi Taleghani et al., 2016)

$$G_c = \frac{1}{2} T_{max} \delta_m^f = \frac{1}{2\gamma} T_{max} \delta_m^0 = \frac{T_{max}^2}{2\gamma K_{coh}} \quad (17)$$

where  $T_{max}$  is the cohesive strength, and  $\gamma$  is the ratio between critical separation at damage initiation and at complete failure. In quasi-static state, the static stress intensity factor (SIF) of mode I fracture can be equal to that of the mode I fracture toughness (Dahi Taleghani et al., 2018). Therefore, the evaluated fracture toughness for the cohesive energy calculated by Eq. (17) can be approximated by

$$K_{IC} = \sqrt{E' G_c} = \sqrt{\frac{E G_c}{1 - \nu^2}} \quad (18)$$

Based on Eqs. (1)–(18), the fracture toughness between the theoretical solution and simulation under pure mode I can be readily compared. The cohesive strength in VDR is set to 6 MPa, which is close to the rock tensile strength of the regular model in previous DEM simulations (Huang et al., 2019). In TDR, the cohesive strength is set to 20

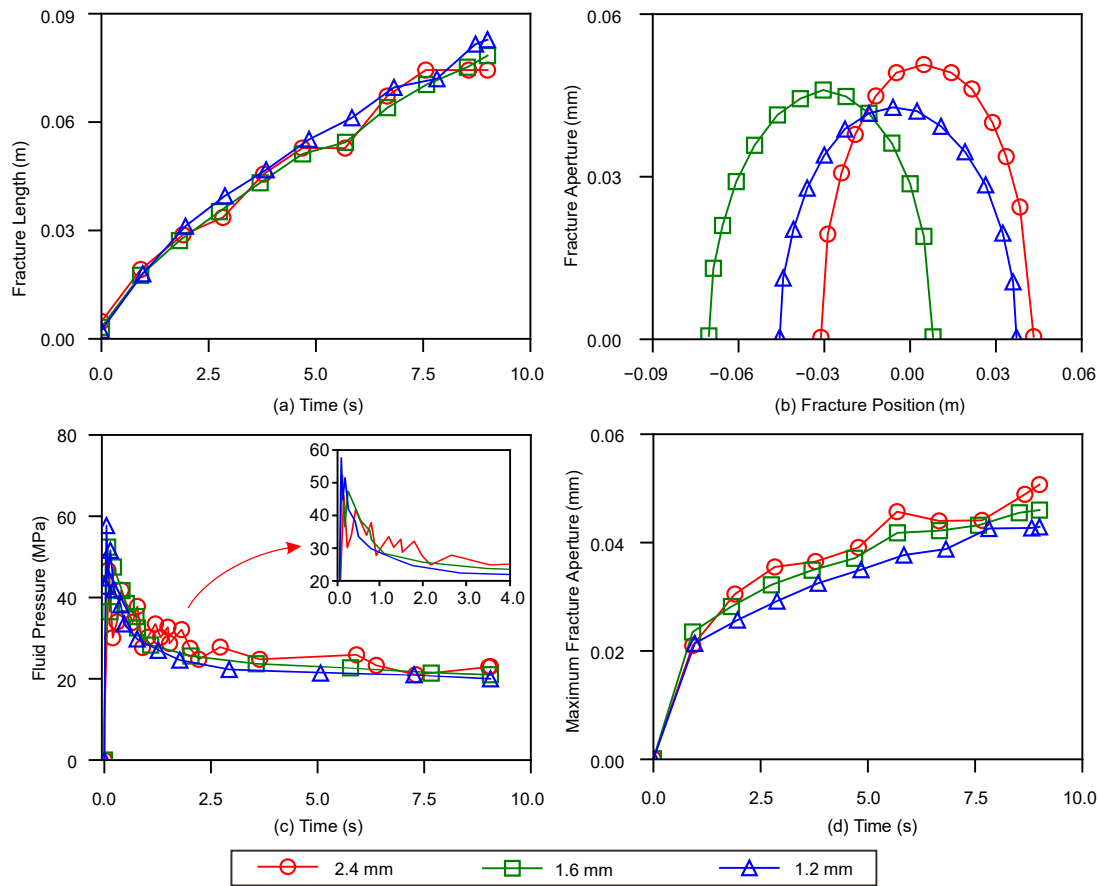


**Fig. 11.** Simulation results of hydraulic fracturing in TDR for the three heterogeneous models of different element size in terms of (a) fracture length versus injection time, (b) fracture aperture versus fracture position, (c) fluid pressure versus injection time, and (d) maximum fracture aperture versus injection time.

MPa, which is higher than that in VDR. The failure displacement in VDR and TDR is set to  $1.0 \times 10^{-5}$  m to make sure that when the aperture of the cohesive element reaches such value, the cohesive element is completely damaged. Then, the cohesive energy and the estimated fracture toughness can be calculated by Eqs. (1)–(18). The cohesive energies in VDR and TDR are chosen to be 30 N/m and 100 N/m, respectively, which are consistent with the general range of rock fracture energy (10–10,000 N/m). In addition, the estimated fracture toughness in VDR and TDR is  $0.98 \text{ MPa}\cdot\text{m}^{0.5}$  and  $1.80 \text{ MPa}\cdot\text{m}^{0.5}$ , respectively. Compared with the fracture toughness applied in the theoretical solutions (Table 1), the estimated fracture toughness in VDR is a slightly higher than that in the theoretical solution, while the estimated fracture toughness in TDR is much lower than that in the theoretical solution. These indicate that the additional parameters of the cohesive elements selected are reasonable. Meanwhile, the above results indicate that the conversion of dynamic fracture toughness by static SIF can infer the reasonable range of parameters in traction separation criterion to a certain extent, but it is not enough to determine the accurate values of each parameter. In addition, according to the Rice's element size evaluation equation ( $l_c = \frac{9\pi}{32} \frac{EG_c}{\sigma_t^2}$ ) (Palmer et al., 1973; Tabiei and Zhang, 2017) and based on the parameters used in the current simulations, the maximum allowed element size in VDR and TDR are respectively 21.72 mm and 6.52 mm. The cohesive element sizes used in the current paper, i.e., 2.4 mm, 1.6 mm, 1.2 mm, are all within the reasonable range. Therefore, we believe our simulation could generate reliable results.

### 3.3. Calibration results

The final stress nephograms for the simulation models in VDR (at 0.1

s) and TDR (at 9 s) are shown in Fig. 5. Please note that due to the small aperture of hydraulic fracture (0–0.12 mm), the aperture shown in the stress nephograms is magnified by 100 times for better visualization. It can be seen from Fig. 5 that the range of stress distribution in VDR is obviously larger than that in TDR, that is, the hydraulic fracture propagation in VDR is more severe than that in TDR. In addition, the final hydraulic fracture morphologies formed in the two regimes are both similar to the elliptical shape in the theoretical KGD model (Dontsov and Peirce, 2015). When the simulation is finished, the fracture length, the maximum fracture aperture, and the relationship between the fracture position and the fracture aperture are obtained to describe the final fracture morphology.

The comparison between the theoretical solutions and the simulation results (homogeneous model) in terms of the variation of hydraulic fracture length and the final fracture morphology (the fracture aperture versus fracture position) in the two regimes are respectively shown in Fig. 6. Fig. 6a & b show a decent match between the simulation results and the theoretical solution in terms of the fracture length evolution with respect to time and the final fracture aperture with respect to location. The results demonstrate the reliability of the FDEM model and the rationality of parameter selection in VDR. In Fig. 6c and d, again, the negligible difference between the theoretical solution and the simulation results demonstrates the model effectiveness in TDR.

## 4. Simulation results and discussions

The calibration presented above verifies the applicability and reliability of our numerical model. As we mentioned earlier, in addition to the rock elastic modulus (controlled by the shape parameter  $\beta$ ), other three possible influencing factors such as the element size  $l_b$ , and the

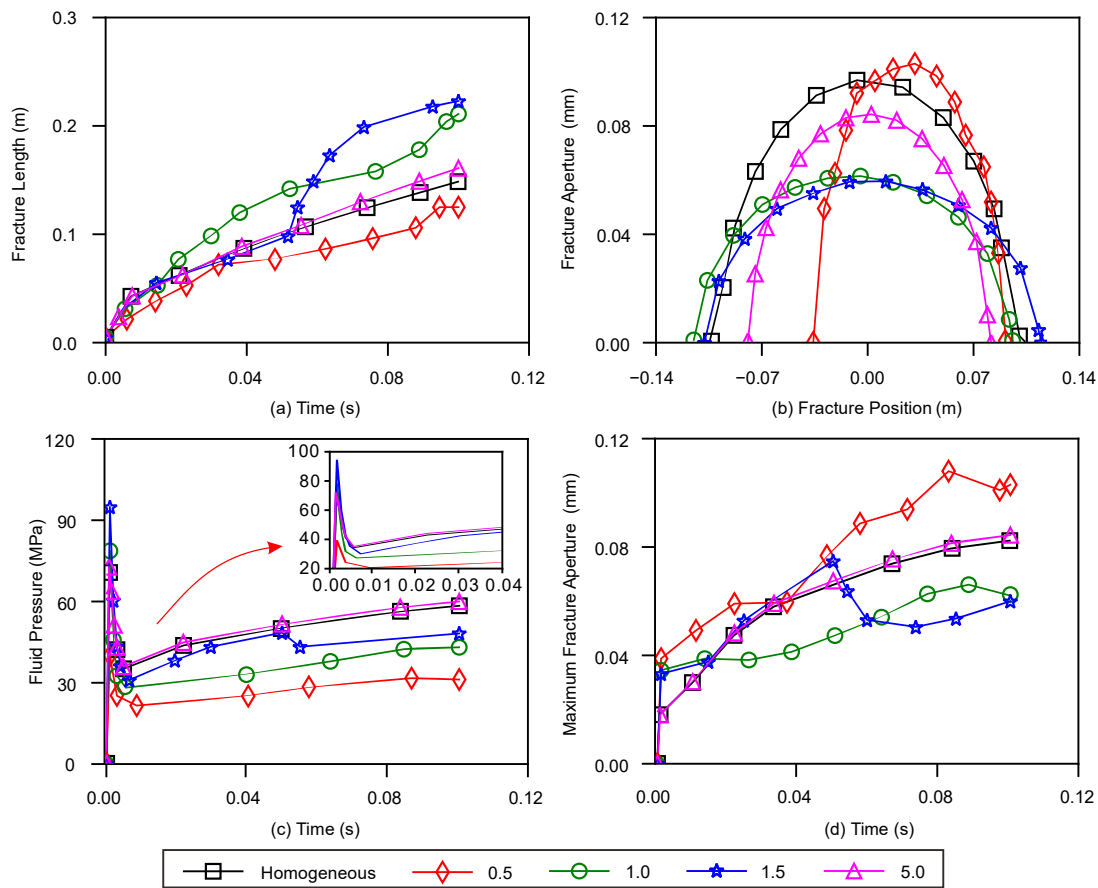


Fig. 12. Simulation results of hydraulic fracturing in VDR for different distribution types of rock elastic modulus in terms of (a) fracture length versus injection time, (b) fracture aperture versus fracture position, (c) fluid pressure versus injection time, and (d) maximum fracture aperture versus injection time.

maximum ( $\sigma_H$ ) and minimum ( $\sigma_h$ ) far-field stress may also affect the hydraulic fracture propagation. In the present analysis, we mainly consider these four influencing factors, and have designed four corresponding groups of rock models to thoroughly investigate their influence on hydraulic fracturing. The combination of these parameters in the four model groups is carefully chosen and sketched in Fig. 7. Please note that the origin (black marker in Fig. 7) represents the initial model parameter setting used for the heterogeneous model, i.e., the shape parameter  $\beta$  is 5.0, the element size  $l_b$  is 2.4 mm, the maximum far-field stress  $\sigma_H$  is 15 MPa, and the minimum far-field stress  $\sigma_h$  is 10 MPa. It is worth mentioning that the simulated homogeneous model used in Section 3.3 is based on the initial model here.

#### 4.1. Influence of element size

To reveal the influence of element size on hydraulic fracturing, three homogeneous and three heterogeneous rock specimens with element sizes of 2.4 mm, 1.6 mm, and 1.2 mm are first prepared (corresponding to the model group shown in blue in Fig. 7). Other parameters are consistent with the initial model (black marker in Fig. 7). The simulation results of these homogeneous and heterogeneous models under the two propagation regimes (i.e., VDR and TDR) are shown in Figs. 8–11.

Fig. 8 presents the simulation results in VDR for the three homogeneous models using different element sizes. It can be seen from Fig. 8 that with the decrease of element size, the fracture length witnesses a slight increase (Fig. 8a), while the fracture aperture decreases (Fig. 8b and d). Meanwhile, the breakdown pressure and propagation pressure seem to have a downward trend. This result indicates that the smaller the element size is, the faster the hydraulic fracture propagates forward (Fig. 8a). Meanwhile, it should be noted that the influence of element

size on hydraulic fracturing in the homogeneous model in VDR is not obvious. The simulation results in VDR for the three heterogeneous models using different element sizes are shown in Fig. 9. In addition to the slightly observable effect on the breakdown pressure, the influence of element size on the variations of fracture length, fracture aperture, and final fracture morphology seems negligible. This may be due to the distribution characteristics of rock elastic modulus, which reduces the influence of element size on hydraulic fracture propagation in VDR. Therefore, it seems acceptable to adopt different element sizes (2.4 mm, 1.6 mm, and 1.2 mm) for both homogeneous and heterogeneous models in VDR.

Fig. 10 and Fig. 11 show the simulation results of hydraulic fracturing in TDR for the three homogeneous and three heterogeneous models respectively using different element size. In Fig. 10, with the reduction of element size, the fracture length increases, while the propagation pressure and the maximum fracture aperture decrease. Meanwhile, it seems that the breakdown pressure is rarely affected by the element size. Besides, Fig. 10 show that the results of the hydraulic fracturing in the homogeneous rock specimens with element size of 1.6 mm and 1.2 mm are relatively close when compared with the model with element size of 2.4 mm. Theoretically, the smaller the element size of the numerical simulation model, the more accurate numerical solution can be obtained. Therefore, the homogeneous rock specimens with element sizes of 1.6 mm and 1.2 mm seem better than that of 2.4 mm in hydraulic fracturing simulation of the homogeneous reservoir in TDR. However, due to the computational expense, appropriate element size is usually selected instead of the minimum element size. Additionally, in the heterogeneous model in TDR (Fig. 11), with the reduction of element size, the effect of element size on fracture length is less obvious (Fig. 11a), while the fluid pressure and maximum fracture aperture

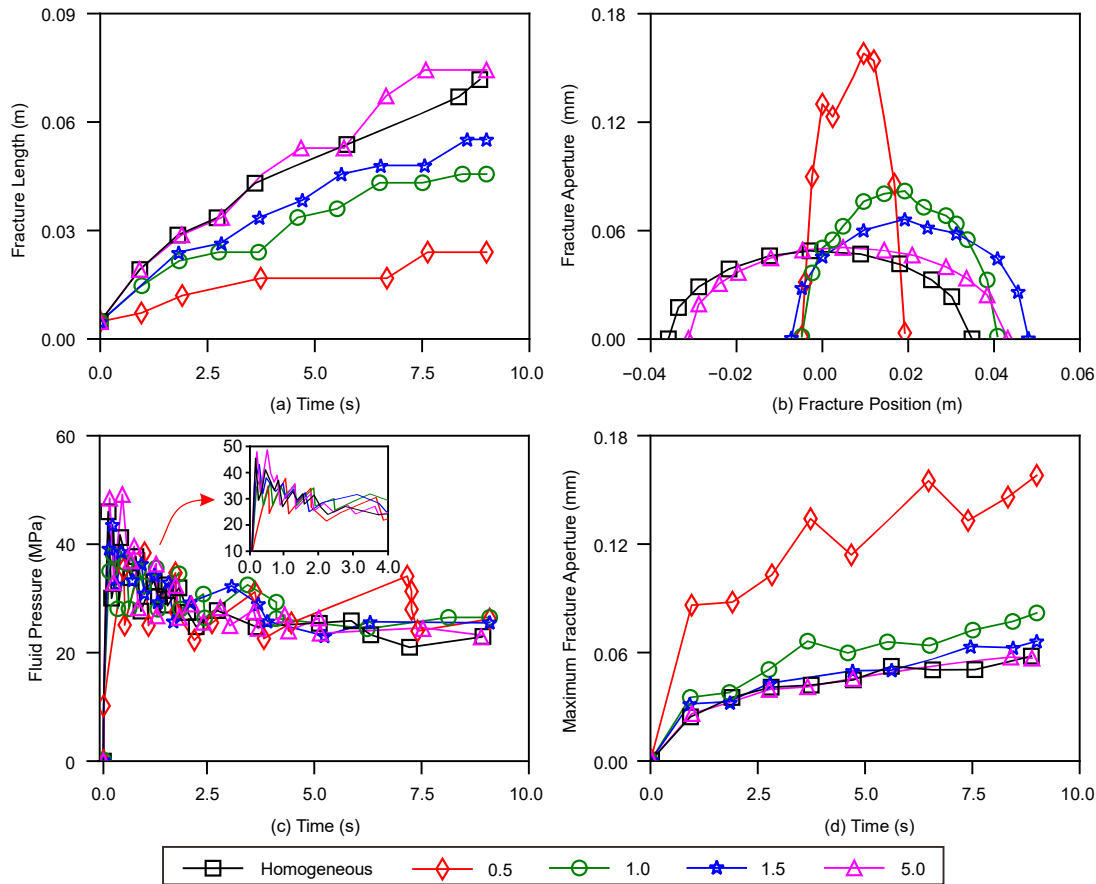


Fig. 13. Simulation results of hydraulic fracturing in TDR for different distribution types of rock elastic modulus in terms of (a) fracture length versus injection time, (b) fracture aperture versus fracture position, (c) fluid pressure versus injection time, and (d) maximum fracture aperture versus injection time.

show a slightly decreasing trend (Fig. 11c & d). Please note that the final fracture morphology in the heterogeneous model in TDR is quite different for the models with different element size (Fig. 11b). Therefore, the optimal element size cannot be determined only by the final fracture morphology in the heterogeneous model in TDR.

Comparing Fig. 8 with Fig. 10, although the influence trend of element size on hydraulic fracturing is generally the same, such influence in TDR is more obvious than that in VDR. Likewise, comparing Fig. 9 with Fig. 11, a similar phenomenon can be found. Additionally, the final fracture morphology in heterogeneous models in TDR shows obvious asymmetric propagation (Fig. 11b). However, this has not been observed in VDR (Fig. 9b). The results indicate that the influence of element size in TDR is more significant than that in VDR, which implies that the hydraulic fracture propagation in TDR is more susceptible to element size. This may be caused by the high injection rate in VDR, and thus at the very beginning of fluid injection, the rocks, especially in places away from the injection point, do not have enough time to respond and therefore are less deformed. As a result, the influence of rock heterogeneity (here mainly controlled by the element size since the heterogeneous rock elastic modulus are assigned in an element-based manner) on the hydraulic fracture propagation in VDR is less apparent than that in TDR. However, as the injection continues, the influence of element size on hydraulic fracture propagation gradually increases.

#### 4.2. Influence of Weibull distribution type

To further investigate the influence of material heterogeneity on hydraulic fracture propagation, four typical Weibull distributions with shape parameters  $\beta$  (i.e. the material homogeneity index) of 0.5, 1.0, 1.5, and 5.0 are used to establish heterogeneous rock models with their rock elastic modulus following different Weibull distribution types (corresponding to the model group shown in magenta in Fig. 7). Other parameters such as the element size and far-field stress are consistent with the initial model (black marker in Fig. 7). In addition, the results of the homogeneous model (Section 3.3) are also presented in the following comparison. The results of the models in VDR and TDR are respectively presented in Fig. 12 and Fig. 13.

Both Fig. 12 and Fig. 13 manifest that the Weibull distribution type of rock elastic modulus has a significant impact on hydraulic fracture propagation in both fracturing control regimes. As shown in Fig. 12, in VDR, for the heterogeneous model with  $\beta = 5.0$ , the variations of fracture length, fluid pressure, and maximum fracture aperture are close to these in the homogeneous model. While with the decrease of material homogeneity index  $\beta$  (i.e., the increase of rock heterogeneity), the variation of fluid pressure in the heterogeneous models seems more deviated from the homogeneous model (Fig. 12c). We can also observe in Fig. 12c that for the model with shape parameter  $\beta = 1.5$  the breakdown pressure could reach over 90 MPa, although the minimum far field stress is merely 10 MPa. This is not uncommon in previous research. For example, in the previous DEM simulation (Huang et al., 2019), when

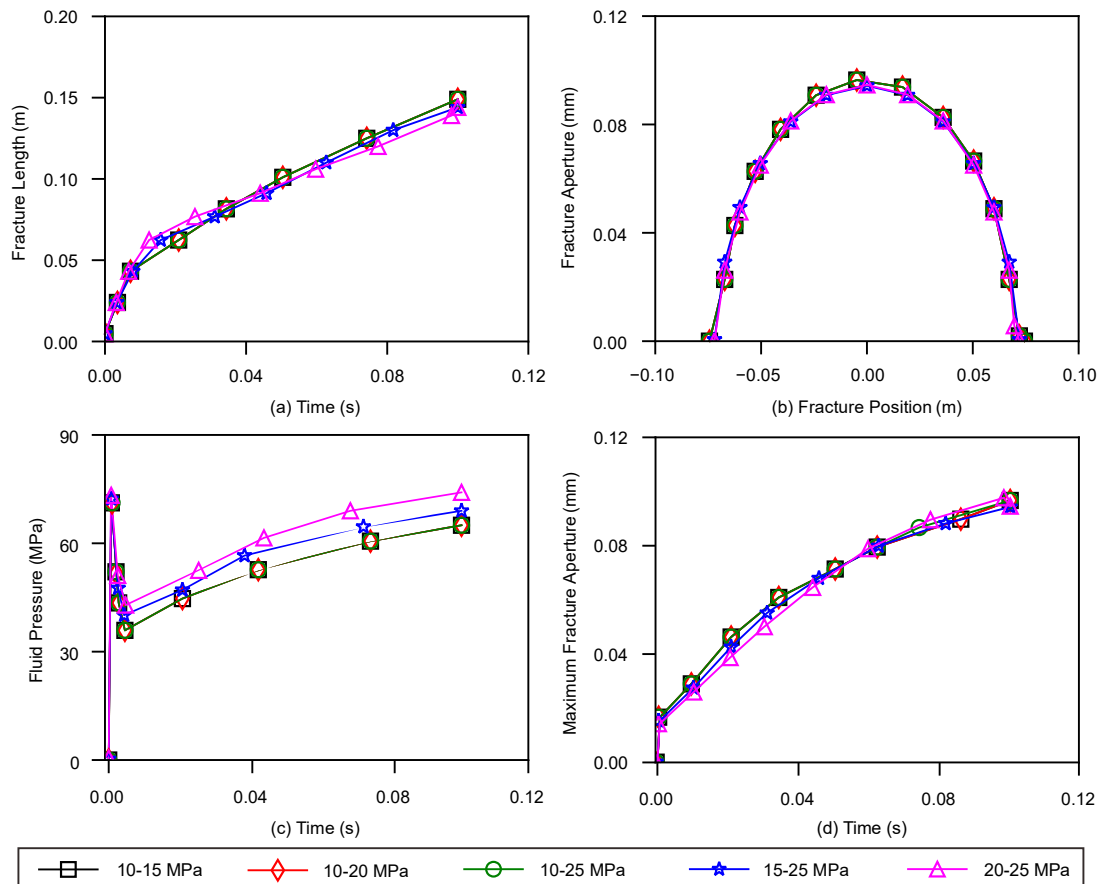


**Fig. 14.** Simulation results of hydraulic fracturing in homogeneous model for different minimum and maximum far-field stress combinations in VDR in terms of (a) fracture length versus injection time, (b) fracture aperture versus fracture position, (c) fluid pressure versus injection time, and (d) maximum fracture aperture versus injection time.

multiple randomly arranged particle specimens are used, the breakdown pressure varies in the range from 60 to 80 MPa. Thus, we speculate that this phenomenon may be caused by the influence of rock elastic modulus distribution, which further enhance the breakdown pressure.

Afterward, the fluid pressure keeps rising, and the propagation pressure for homogeneous model and the heterogeneous model with shape parameters  $\beta = 1.5$  reach  $\sim 60$  MPa (Fig. 12c). A similar phenomenon can be found in a previous true triaxial fracturing experiments (Deng et al., 2018a; Deng et al., 2018b). This may be caused by the short fracturing time (0.1 s in the current VDR analysis), which is possible to result in a much greater fluid injection rate than the absorption capacity. Additionally, with the decrease of material homogeneity index  $\beta$ , the propagation pressure in VDR decreases. This could be caused by the fact that the hydraulic fractures may be more prone to propagate along the direction of weak deformation resistance of rock and thus causes a decreasing propagation pressure. However, when the material homogeneity index  $\beta$  increases, no specific increase or decrease trend of the fracture length, the final fracture morphology and the maximum fracture aperture in VDR has been observed (Fig. 12a, b, and d). This indicates a certain randomness in the hydraulic fracture propagation under the influence of heterogeneity.

In Fig. 13, similarly, the results of the heterogeneous model with  $\beta = 5.0$  is very close to the homogeneous model. The changing trend of the propagation pressure with respect to the homogeneity index  $\beta$  in TDR is not obvious (Fig. 13c). However, with the decrease of  $\beta$ , the fracture length has a significant decline in TDR (Fig. 13a). While the maximum fracture aperture in TDR has a significant increase (Fig. 13d). These results denotes that the influencing degree of material homogeneity on hydraulic fracturing in different regimes is different. For VDR with high

injection rate and short injection duration, the stress change caused by fluid injection can also be affected by the stiff rock elements even at the beginning of injection. However, also due to the short injection duration in VDR, the hydraulic fracture opening mainly just affects the near-field stress redistribution. On the contrary, the hydraulic fracturing in TDR can influence both the near-field and far-field stress redistributions. As a result, we can observe an obvious trend regarding the influence of the material homogeneity index  $\beta$  on fluid pressure in VDR, while such influence in TDR is chaotic. In addition, a distinct trend of the influence of material homogeneity index  $\beta$  on the evolution of fracture length and maximum fracture aperture in TDR can be observed.

The displacement of hydraulic fracture position and asymmetrical propagation also appear in Fig. 12b. It is worth mentioning that no clear trend has been found for the influence of material homogeneity index  $\beta$  on the final fracture morphology, except for models in VDR with  $\beta = 0.5$  and 5.0 (Fig. 12b) in which the final hydraulic fracture morphology is apparently different from those with  $\beta = 1.0$  and 1.5. Interestingly, in VDR, the final fracture morphology of  $\beta = 1.0$  seems close to that of  $\beta = 1.5$ , while the hydraulic fracture length, fracture aperture, and fluid pressure have obvious differences. This phenomenon can also be observed in TDR (Fig. 13). In addition, when  $\beta = 0.5, 1.5$  and 5.0 in TDR, the position of the maximum fracture aperture does not occur near the injection point, which can be observed in Fig. 13b. Therefore, we speculate that the heterogeneous models with  $\beta = 1.0$  and 1.5 may have similar mechanical properties. However, the current characterization parameter (the material homogeneity index  $\beta$ ) may not be able to fully capture the factor that affects the hydraulic fracturing in heterogeneous rocks. Therefore, a clear relationship between the heterogeneity characterization parameters (e.g., the material homogeneity index  $\beta$ ) and the

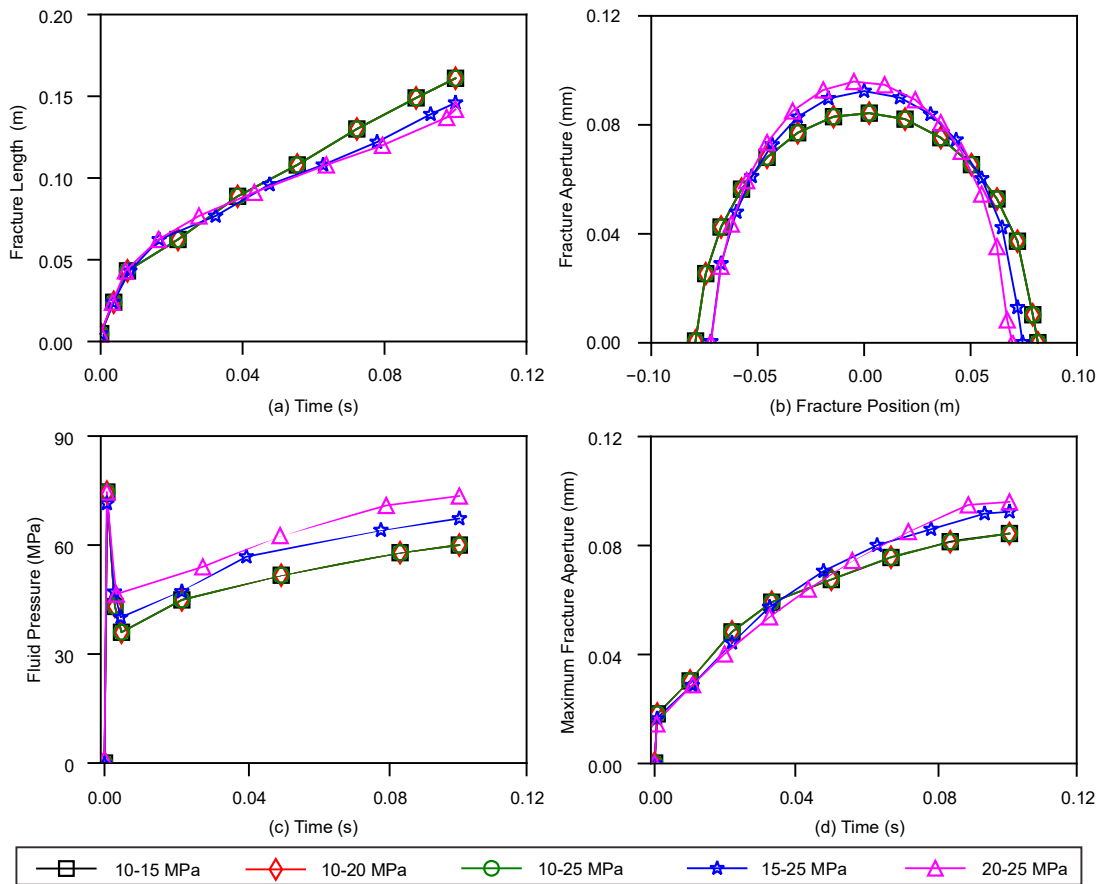


**Fig. 15.** Simulation results of hydraulic fracturing in heterogeneous model for different minimum and maximum far-field stress combinations in VDR in terms of (a) fracture length versus injection time, (b) fracture aperture versus fracture position, (c) fluid pressure versus injection time, and (d) maximum fracture aperture versus injection time.

hydraulic fracturing effect evaluation parameters (fracture length, maximum fracture aperture, fluid pressure, and the final fracture morphology) has not been found. Based on the above analysis, it is necessary to further study the influence of the proportion of soft rock elements to stiff rock elements on the results for heterogeneous models.

### 4.3. Influence of far-field stress

The far-field stress condition (i.e., boundary loadings) has not been considered in the formula of propagation regimes (Dontsov, 2017; Huang et al., 2019; Zhang and Dontsov, 2018); however, it plays an important role in hydraulic fracturing. Similar to the previous research (Huang et al., 2019), the maximum far-field stress used here is first increased from 15 MPa to 25 MPa (corresponding to the model group shown in red in Fig. 7), then the minimum far-field stress is increased from 10 MPa to 20 MPa (corresponding to the model group shown in green in Fig. 7). Other parameters such as the element size are consistent with the initial model (black marker in Fig. 7). We first present the results of both the homogeneous and heterogeneous models in VDR, and then followed by the models in TDR.

For the homogeneous models in VDR (Fig. 14), when maintaining a constant maximum far-field stress (i.e.,  $\sigma_H = 25$  MPa), with the increase of minimum far-field stress, the breakdown pressure increases from 71.21 and 72.18 to 74.94 MPa (Fig. 14c). While when keeping the minimum far-field stress constant (i.e.,  $\sigma_h = 10$  MPa) and increasing the maximum far-field stress from 15 to 25 MPa, the breakdown pressure has no apparent change, i.e., changing from about 71.202 and 71.205 to 71.208 MPa (Fig. 14c). This indicates that the breakdown pressure during fracturing may be more susceptible to the minimum far-

field stress than the maximum far-field stress, which is consistent with the previous researches (Ju et al., 2016; Peng et al., 2017). Additionally, in Fig. 14a, b, and d, the results show that both the maximum and minimum far-field stresses have no distinct effect on the evolution of hydraulic fracture morphology (fracture length, maximum fracture aperture, and the final fracture morphology).

When the material heterogeneity is considered, with the increase of minimum far-field stress (the maximum far-field stress is maintained constant), the fracture length reduces (Fig. 15a), while the maximum fracture aperture display the opposite trend (Fig. 15d). The change of breakdown pressure in terms of minimum and maximum far-field stress shown in Fig. 15c is similar to the results of the homogeneous models in VDR in Fig. 14c. Afterward, the fluid pressure for 20–25 MPa in VDR rises above the breakdown pressure (Fig. 14c and Fig. 15c), while it does not occur in TDR (Fig. 16c and Fig. 17c) and other far-field stress conditions. Therefore, we speculate that this may be due to high far-field stress and a large amount of fluid injection in a short time. Compared with Fig. 14a, c, and d, the results denote that the influence of far-field stress on the homogeneous and heterogeneous models in VDR is different. Generally, the fluid pressure increases with the increasing minimum far-field stress for both the homogeneous and heterogeneous models in VDR, which means that the far-field stress is also an important factor for hydraulic fracturing. However, in homogeneous model, the influence of the minimum far-field stress on the fracture length, the maximum fracture aperture, and the final fracture morphology is negligible; while its effect in heterogeneous model cannot be simply ignored. The results indicate that under the influence of rock heterogeneity, the effect of far-field stress on hydraulic fracturing of reservoir rock will also vary. Therefore, it is necessary to comprehensively

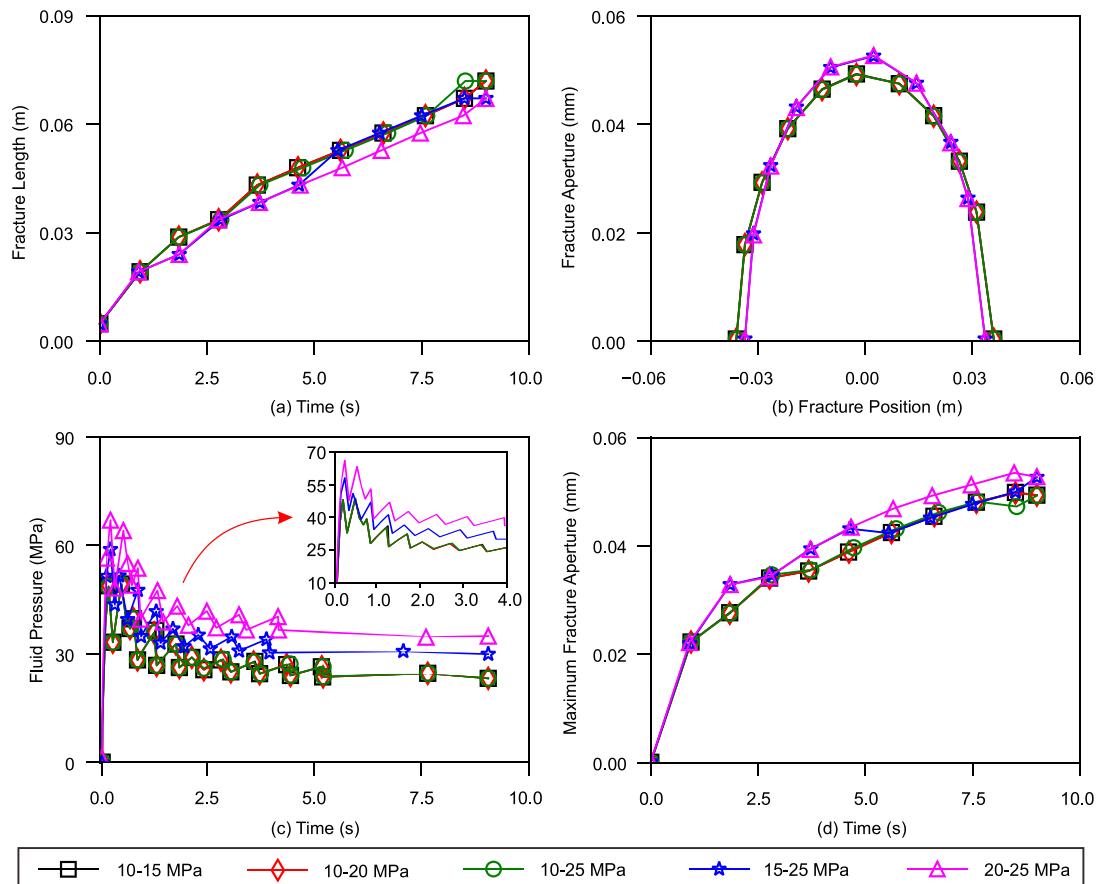


**Fig. 16.** Simulation results of hydraulic fracturing in homogeneous model for different minimum and maximum far-field stress combinations in TDR in terms of (a) fracture length versus injection time, (b) fracture aperture versus fracture position, (c) fluid pressure versus injection time, and (d) maximum fracture aperture versus injection time.

consider the influence of far-field stress and heterogeneous characteristics in hydraulic fracturing simulations.

Fig. 16 and Fig. 17 depict the simulation results of hydraulic fracturing in homogeneous and heterogeneous model respectively for the various far-field stress combinations in TDR. When the maximum far-field stress is constant, the fluid pressure increases with the increasing minimum far-field stress, which is consistent with the previous models in TDR. For the homogeneous models in TDR, with the increasing minimum far-field stress, the fracture length decreases, while the fracture aperture increases. While for the heterogeneous models in TDR, these changing trends have obvious fluctuations, which has not been found in VDR. These results denote that the influence of far-field stress on fluid pressure and fracture morphology evolution in homogeneous and heterogeneous models under different propagation regimes is different. Generally, hydraulic fracture propagation in TDR is more susceptible to far-field stress than that in VDR, and hydraulic fracture propagation is more susceptible to the minimum far-field stress than the maximum far-field stress.

## 5. Conclusions

This paper discusses the influence of rock heterogeneity on hydraulic fracture propagation under both VDR and TDR using two-dimensional FDEM. Both the homogeneous model using a universal rock elastic modulus and the heterogeneous model using the Weibull-distributed rock elastic modulus are realized. The variability of fluid pressure, fracture length, maximum fracture aperture, and the final fracture morphology is evaluated.

The results in Sections 3 validate the reliability and accuracy of our

simulation models and the rationality of model parameters. Meanwhile, the parameter analysis shows that the previous theoretical equations can be used as a preliminary evaluation of the simulation parameters, but still needs further improvement. The “jump” phenomenon has been observed in TDR caused by high fracture toughness, and asymmetrical dynamic propagation affected by rock heterogeneity appears in TDR. However, this phenomenon is not obvious in VDR. Therefore, the hydraulic fracture propagation in TDR is more susceptible to the influence of rock heterogeneity than that in VDR. Similar conclusions have been found in the subsequent parametric analysis.

The hydraulic fracture propagation in TDR is more sensitive to element size than that in VDR. Meanwhile, under the influence of rock heterogeneity, the effect of element size on hydraulic fracture propagation in different control mechanisms is different. In VDR, the heterogeneity reduces the effect of element size on hydraulic fracture propagation; while in TDR, the heterogeneity increases the uncertainty of the influence of element size. The distribution type of rock elastic modulus has a significant impact on the hydraulic fracture propagation in both control regimes. Common characteristics and fluctuations have been found in the hydraulic fracturing effect of rocks under different Weibull distribution types. When  $\beta = 0.5$  in TDR, the position of the maximum fracture aperture deviates away from the injection point. Hydraulic fracture propagation in TDR is more vulnerable to the far-field stress than that in VDR, and the influence of minimum far-field stress on hydraulic fracture propagation is more significant than the maximum far-field stress. Furthermore, the stronger the rock heterogeneity is, the more obvious the influence would be. Additionally, the minimum far-field stress has slightly effect on fracture length and maximum fracture aperture; however, its influence on fluid pressure is

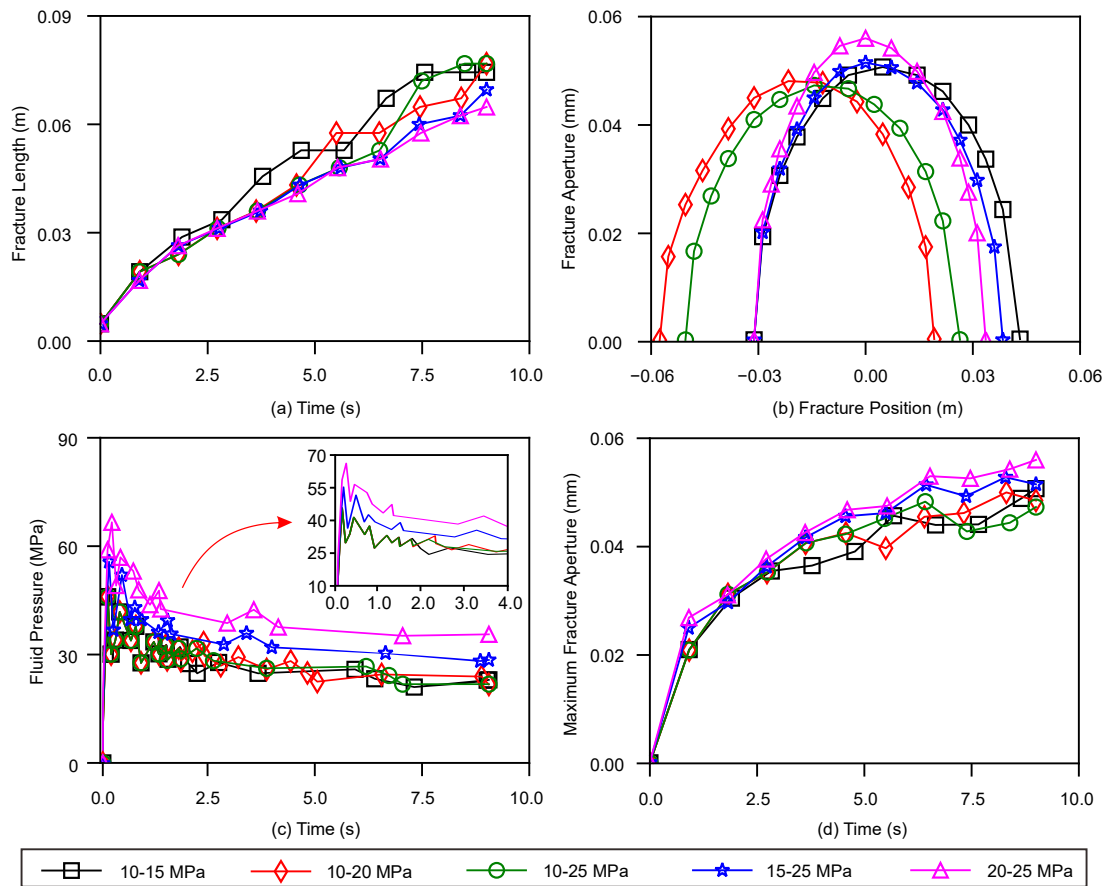


Fig. 17. Simulation results of hydraulic fracturing in heterogeneous model for different minimum and maximum far-field stress combinations in TDR in terms of (a) fracture length versus injection time, (b) fracture aperture versus fracture position, (c) fluid pressure versus injection time, and (d) maximum fracture aperture versus injection time.

significant.

## 6. Data availability

The data used to support the findings of this study are available from the corresponding author upon request.

## 7. Funding statement

The authors gratefully acknowledge the financial support given by

the National Natural Science Foundation of China (42004036, 51804049, and 51874053), and the Postdoctoral Science Foundation of State Key Laboratory of Coal Mine Disaster Dynamics and Control (2011DA105287-BH201905).

## Declaration of Competing Interest

The authors declare that they have no known competing financial interests or personal relationships that could have appeared to influence the work reported in this paper.

## Appendix A. Coupled deformation-diffusion phenomena

The fluid diffusion in porous media obeys the Darcy's law (Wang, 2019)

$$\mathbf{q}_m = -\frac{k}{\mu} \nabla p_m \tag{A.1}$$

where  $k$  represents the permeability tensor,  $\mathbf{q}_m$  is the fluid flux velocity vector in the porous media, and  $p_m$  represents the pore pressure in the formation. In fluid-filled porous media, the total stresses,  $\sigma_{ij}$ , are related to the effective stresses,  $\sigma'_{ij}$ , by (Biot, 1941)

$$\sigma_{ij} = \sigma'_{ij} + \alpha p_m \tag{A.2}$$

where  $p_m$  is the pore pressure in the formation, and  $\alpha$  is the poroelastic constant assumed to be 1 based on a previous study (Wang, 2016). Then, the equilibrium equation of poroelasticity in the form of the virtual work principle for the volume under its current deformation at time  $t$  can be written as (Wang, 2016)

$$\int_V (\sigma' + p_m \mathbf{I}) : \delta \varepsilon dV = \int_S \mathbf{t} \delta v dS + \int_V \mathbf{f} \delta v dV \tag{A.3}$$

where  $\sigma'$  is the effective stress,  $\mathbf{I}$  is the identity matrix,  $\mathbf{t}$  and  $\mathbf{f}$  are the surface traction per unit area and body force per unit volume, respectively,  $\delta$  denotes the virtual component,  $\delta \varepsilon$  is the virtual rate of deformation; and  $\delta v$  is the virtual displacement. The porous medium is thus modeled by attaching the finite element mesh to the solid phase, which allows the liquid to flow through. A continuity equation is required for the fluid, equating the rate of increase in fluid volume stored at a point to the rate of volume of fluid flowing into the point within the time increment (Wang, 2019):

$$\frac{d}{dt} \left( \int_V \rho_f \phi dV \right) + \int_S \rho_f \phi \mathbf{n} q_m dS = 0 \tag{A.4}$$

where  $\rho_f$  and  $\phi$  are the density of the fluid and porosity of the porous media, respectively, and  $\mathbf{n}$  is the outward normal to surface  $S$ .

Because the fracture propagation simulation has the characteristics of strong nonlinearity and convergence difficulty, the simulation results in this paper are obtained by Newton iterative calculation. The time step will automatically increase or decrease according to the convergence criterion. It not only saves the calculation time, but also ensures the accuracy of the simulation results.

**Appendix B. . Parameter selection in TDR**

It was mentioned in previous DEM simulation studies (Huang et al., 2019) that the  $K_{IC}$  in the theoretical solution used to compare the simulation model results in TDR increases from 1.63 MPa·m<sup>0.5</sup> to 2.10 MPa·m<sup>0.5</sup>. Therefore, two simulation models are tested to pre-evaluate the characteristics of hydraulic fracture propagation in TDR. The main parameters of cohesive element in the first simulation test are determined as follows. The cohesive strength is 12 MPa; the failure displacement is 1e-5 m; the fluid leak-off is ignored. Based on Eqs. (1)–(18), the cohesive energy is 60 N/m and the estimated fracture toughness is 1.39 MPa·m<sup>0.5</sup>. The fracture toughness in the theoretical solution is 1.63 MPa·m<sup>0.5</sup>. Meanwhile, the cohesive strength is close to the macro tensile strength of 13 MPa in the previous DEM simulations (Huang et al., 2019), and the cohesive energy is within the range of 10–10,000 N/m. The simulation results are shown in Fig. B.1. In the second simulation test, only the cohesive strength is changed to 85 MPa. Based on Eqs. (1)–(18), the cohesive energy is 425 N/m and the estimated fracture toughness is 3.7 MPa·m<sup>0.5</sup>. The cohesive energy is close to the parameter

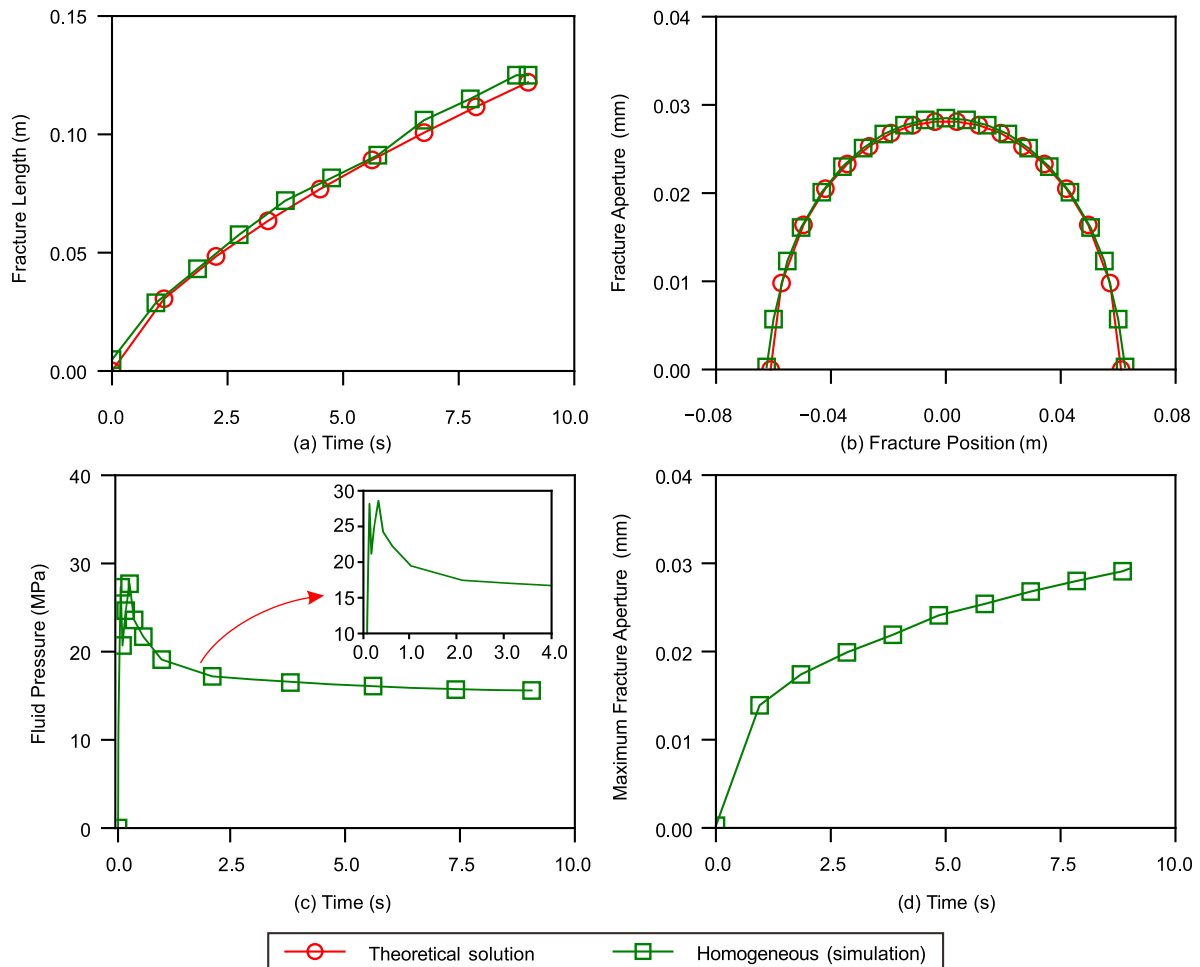


**Fig. B1.** The first simulation test results. Comparison between the theoretical solution and the numerical solution in terms of (a) fracture length versus injection time, (b) fracture aperture versus fracture position, and the simulation results of the homogeneous heterogeneous model in terms of (c) fluid pressure of inject point versus injection time, and (d) maximum fracture aperture versus injection time.

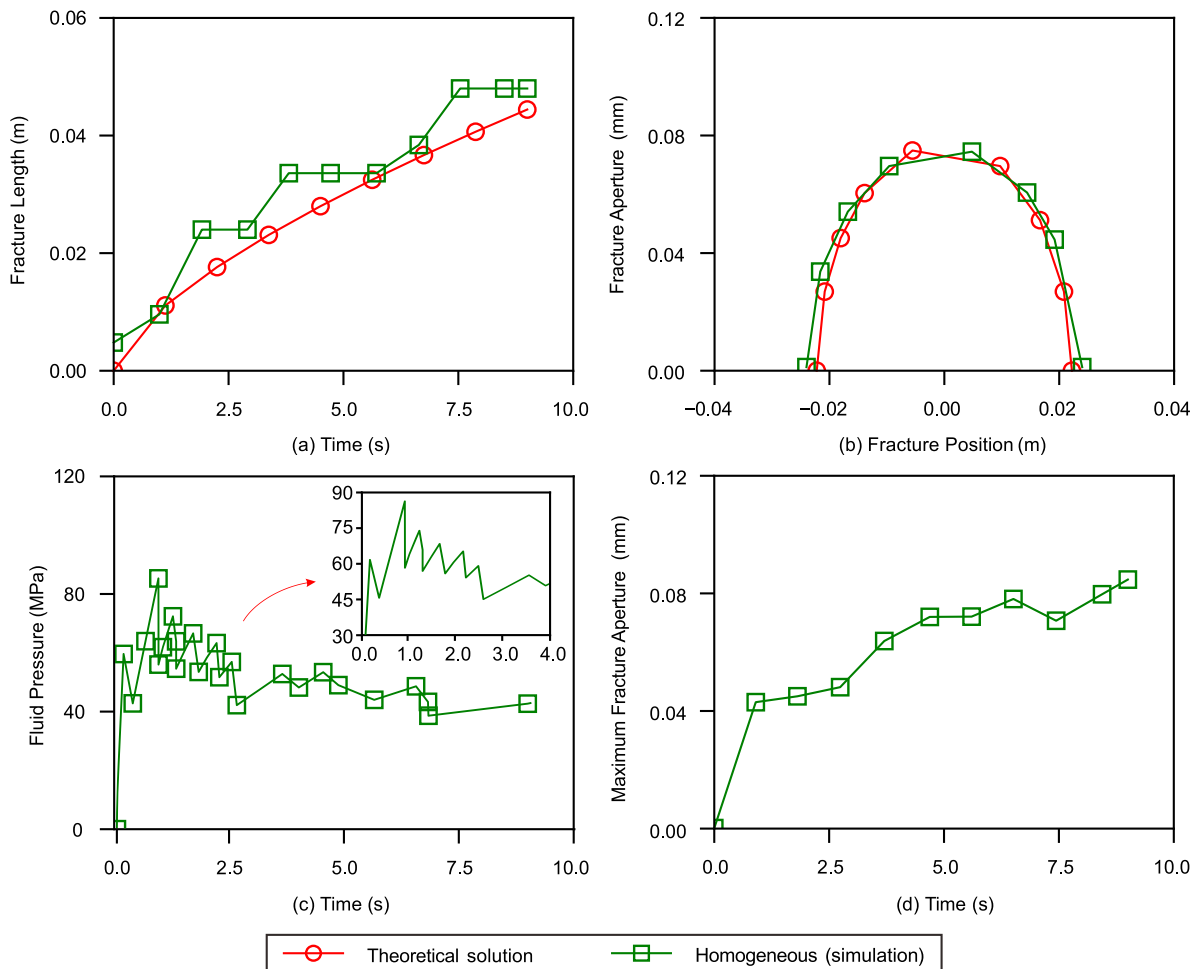


**Fig. B2.** The second simulation test results. Comparison between the theoretical solution and the numerical solution in terms of (a) fracture length versus injection time, (b) fracture aperture versus fracture position, and the simulation results of the homogeneous heterogeneous model in terms of (c) fluid pressure of inject point versus injection time, and (d) maximum fracture aperture versus injection time.

range in the previous simulations (Dahi Taleghani et al., 2018; Dahi Taleghani et al., 2016), while the cohesive strength is higher than the general rock macro tensile strength. Meanwhile, the  $K_{IC}$  in the theoretical solution is  $7.42 \text{ MPa}\cdot\text{m}^{0.5}$  ( $\log_{10}(K_m)$  is approximately 1.53, thus it belongs to TDR), which is much higher than the general rock fracture toughness. The simulation results are shown in Fig. B.2.

The comparison between the homogeneous model and the analytical solution demonstrates the reliability of the simulation models. In Fig. B.1, the variation of hydraulic fracture length, fluid pressure, and the maximum fracture aperture are close to smooth curves. In Fig. B.2, the variation of hydraulic fracture length, fluid pressure, and maximum fracture aperture is tortuous. These results indicate that the results of the second test have greater fluctuation than those of the first test. Generally, these fluctuations can be considered to be caused by the unstable propagation of fractures (Wong et al., 2014), which leads to the change of fracture energy required for each time the fracture propagates forward. Meanwhile, similar to the force–displacement curve, the fluid pressure curve in the process of hydraulic fracture propagation has also become tortuous. This phenomenon was defined as a “jump” phenomenon in previous studies (Dong et al., 2021; Liu et al., 2020). It should be noted that the theoretical solution parameters in Fig. B.2 are obtained by actual derivation. Therefore, the fracture morphology evolution parameters and fluid pressure in Fig. B.2a, c, and d indicate that the hydraulic fracture propagation in TDR may have obvious “jump” phenomena (Dong et al., 2021; Liu et al., 2020). However, the cohesive strength and estimated fracture toughness in the second simulation test is much higher than the general scope, so  $3.6 \text{ MPa}\cdot\text{m}^{0.5}$  (within  $1.63\text{--}7.42 \text{ MPa}\cdot\text{m}^{0.5}$ , and  $K_m$  is 16.4) is selected as cohesive strength for TDR.

## References

- Adachi, J., Siebrits, E., Peirce, A., Desroches, J., 2007. Computer simulation of hydraulic fractures. *Int. J. Rock Mech. Min. Sci.* 44, 739–757.
- Biot, M.A., 1941. General Theory of Three-Dimensional Consolidation. *J. Appl. Phys.* 12, 155–164.
- Carrier, B., Granet, S., 2012. Numerical modeling of hydraulic fracture problem in permeable medium using cohesive zone model. *Eng. Fract. Mech.* 79, 312–328.
- Cheng, W., Wang, R., Jiang, G., Xie, J., 2017. Modelling hydraulic fracturing in a complex-fracture-network reservoir with the DDM and graph theory. *J. Nat. Gas Sci. Eng.* 47, 73–82.

- Dahi Taleghani, A., Gonzalez-Chavez, M., Yu, H., Asala, H., 2018. Numerical simulation of hydraulic fracture propagation in naturally fractured formations using the cohesive zone model. *J. Petrol. Sci. Eng.* 165, 42–57.
- Dahi Taleghani, A., Gonzalez, M., Shojaei, A., 2016. Overview of numerical models for interactions between hydraulic fractures and natural fractures: Challenges and limitations. *Comput. Geotech.* 71, 361–368.
- Deng, B., Yin, G., Li, M., Zhang, D., Lu, J., Liu, Y., Chen, J., 2018a. Feature of fractures induced by hydrofracturing treatment using water and L-CO<sub>2</sub> as fracturing fluids in laboratory experiments. *Fuel* 226, 35–46.
- Deng, B., Yin, G., Zhang, D., Li, M., Liu, Y., Lu, J., 2018b. Experimental investigation of fracture propagation induced by carbon dioxide and water in coal seam reservoirs. *Powder Technol.* 338, 847–856.

- Detournay, E., 2004. Propagation Regimes of Fluid-Driven Fractures in Impermeable Rocks. *Int. J. Geomech.* 4, 35–45.
- Detournay, E., 2016. Mechanics of Hydraulic Fractures. *Annu. Rev. Fluid Mech.* 48, 311–339.
- Dong, J.-N., Yuan, G.-J., Wang, X.-Y., Chen, M., Jin, Y., Zeng, C., Zaman, M., 2021. Experimental study of multi-timescale crack blunting in hydraulic fracture. *Pet. Sci.* 18, 234–244.
- Dontsov, E.V., 2017. An approximate solution for a plane strain hydraulic fracture that accounts for fracture toughness, fluid viscosity, and leak-off. *Int. J. Fract.* 205, 221–237.
- Dontsov, E.V., Peirce, A.P., 2015. Proppant transport in hydraulic fracturing: Crack tip screen-out in KGD and P3D models. *Int. J. Solids Struct.* 63, 206–218.
- Dontsov, E.V., Peirce, A.P., 2016. Comparison of toughness propagation criteria for blade-like and pseudo-3D hydraulic fractures. *Eng. Fract. Mech.* 160, 238–247.
- Dontsov, E.V., Suarez-Rivera, R., 2020. Propagation of multiple hydraulic fractures in different regimes. *Int. J. Rock Mech. Min. Sci.* 128, 104270.
- Doughty, C., Long, J.C.S., Hestir, K., Benson, S.M., 1994. Hydrologic characterization of heterogeneous geologic media with an inverse method based on iterated function systems. *Water Resour. Res.* 30, 1721–1745.
- Geertsma, J., De Klerk, F., 1969. A Rapid Method of Predicting Width and Extent of Hydraulically Induced Fractures. *SPE-2458-PA* 21, 1571–1581.
- Guo, J., Zhao, X., Zhu, H., Zhang, X., Pan, R., 2015. Numerical simulation of interaction of hydraulic fracture and natural fracture based on the cohesive zone finite element method. *J. Nat. Gas Sci. Eng.* 25, 180–188.
- Huang, L., Liu, J., Zhang, F., Dontsov, E., Damjanac, B., 2019. Exploring the influence of rock inherent heterogeneity and grain size on hydraulic fracturing using discrete element modeling. *Int. J. Solids Struct.* 176–177, 207–220.
- Ju, Y., Liu, P., Chen, J., Yang, Y., Ranjith, P.G., 2016. CDEM-based analysis of the 3D initiation and propagation of hydrofracturing cracks in heterogeneous glutenites. *J. Nat. Gas Sci. Eng.* 35, 614–623.
- Knight, E.E., Rougier, E., Lei, Z., Euser, B., Chau, V., Boyce, S.H., Gao, K., Okubo, K., Froment, M., 2020. HOSS: an implementation of the combined finite-discrete element method. *Computational Particle Mechanics* 7, 765–787.
- Latham, J.-P., Xiang, J., Belayneh, M., Nick, H.M., Tsang, C.-F., Blunt, M.J., 2013. Modelling stress-dependent permeability in fractured rock including effects of propagating and bending fractures. *Int. J. Rock Mech. Min. Sci.* 57, 100–112.
- Lecampion, B., Desroches, J., 2015. Simultaneous initiation and growth of multiple radial hydraulic fractures from a horizontal wellbore. *J. Mech. Phys. Solids* 82, 235–258.
- Lei, Q., Gao, K., 2018. Correlation Between Fracture Network Properties and Stress Variability in Geological Media. *Geophys. Res. Lett.* 45, 3994–4006.
- Lei, Q., Gao, K., 2019. A numerical study of stress variability in heterogeneous fractured rocks. *Int. J. Rock Mech. Min. Sci.* 113, 121–133.
- Lei, Z., Rougier, E., Knight, E.E., Munjiza, A., 2014. A framework for grand scale parallelization of the combined finite discrete element method in 2d. *Computational Particle Mechanics* 1, 307–319.
- Lei, Z., Rougier, E., Munjiza, A., Viswanathan, H., Knight, E.E., 2019. Simulation of discrete cracks driven by nearly incompressible fluid via 2D combined finite-discrete element method. *Int. J. Numer. Anal. Meth. Geomech.* 43, 1724–1743.
- Li, M., Guo, P., Stolle, D.F.E., Liang, L., Shi, Y., 2020. Modeling hydraulic fracture in heterogeneous rock materials using permeability-based hydraulic fracture model. *Underground Space* 5, 167–183.
- Lisjak, A., Liu, Q., Zhao, Q., Mahabadi, O.K., Grasselli, G., 2013. Numerical simulation of acoustic emission in brittle rocks by two-dimensional finite-discrete element analysis. *Geophys. J. Int.* 195, 423–443.
- Liu, C., Bai, R., Lei, Z., Di, J., Dong, D., Gao, T., Jiang, H., Yan, C., 2020. Study on mode-I fracture toughness of composite laminates with curved plies applied by automated fiber placement. *Mater. Des.* 195, 108963.
- Liu, P., Ju, Y., Gao, F., Ranjith, P.G., Zhang, Q., 2018. CT Identification and Fractal Characterization of 3-D Propagation and Distribution of Hydrofracturing Cracks in Low-Permeability Heterogeneous Rocks. *J. Geophys. Res. Solid Earth* 123, 2156–2173.
- Ma, G., Zhang, Y., Zhou, W., Ng, T.-T., Wang, Q., Chen, X., 2018. The effect of different fracture mechanisms on impact fragmentation of brittle heterogeneous solid. *Int. J. Impact Eng.* 113, 132–143.
- Munjiza, A.A., 2004. The combined finite-discrete element method. John Wiley & Sons.
- Nolte, K.G., 1986. A General Analysis of Fracturing Pressure Decline With Application to Three Models. *SPE-12941-PA* 1, 571–583.
- Palmer, A.C., Rice, J.R., Hill, R., 1973. The growth of slip surfaces in the progressive failure of over-consolidated clay. *Proceedings of the Royal Society of London. A. Mathematical and Physical Sciences* 332, 527–548.
- Peng, P., Ju, Y., Wang, Y., Wang, S., Gao, F., 2017. Numerical analysis of the effect of natural microcracks on the supercritical CO<sub>2</sub> fracturing crack network of shale rock based on bonded particle models. *Int. J. Numer. Anal. Meth. Geomech.* 41, 1992–2013.
- Rougier, E., Munjiza, A., Lei, Z., Chau, V.T., Knight, E.E., Hunter, A., Srinivasan, G., 2020. The combined plastic and discrete fracture deformation framework for finite-discrete element methods. *Int. J. Numer. Meth. Eng.* 121, 1020–1035.
- Salimzadeh, S., Khalili, N., 2015. A three-phase XFEM model for hydraulic fracturing with cohesive crack propagation. *Comput. Geotech.* 69, 82–92.
- Salimzadeh, S., Usui, T., Paluszny, A., Zimmerman, R.W., 2017. Finite element simulations of interactions between multiple hydraulic fractures in a poroelastic rock. *Int. J. Rock Mech. Min. Sci.* 99, 9–20.
- Schwalbe, K.-H., Scheider, I., Cornec, A., 2013. Introduction, Guidelines for Applying Cohesive Models to the Damage Behaviour of Engineering Materials and Structures. Springer, Berlin Heidelberg, Berlin, Heidelberg, pp. 3–15.
- Tabiei, A., Zhang, W., 2017. Cohesive element approach for dynamic crack propagation: Artificial compliance and mesh dependency. *Eng. Fract. Mech.* 180, 23–42.
- Valliappan, V., Remmers, J.J.C., Barnhoorn, A., Smeulders, D.M.J., 2017. Hydraulic fracturing in anisotropic and heterogeneous rocks. 6th Biot Conference on Poromechanics. American Society of Civil Engineers (ASCE).
- Wang, H., 2016. Numerical investigation of fracture spacing and sequencing effects on multiple hydraulic fracture interference and coalescence in brittle and ductile reservoir rocks. *Eng. Fract. Mech.* 157, 107–124.
- Wang, H., 2019. Hydraulic fracture propagation in naturally fractured reservoirs: Complex fracture or fracture networks. *J. Nat. Gas Sci. Eng.* 68, 102911.
- Wong, K.J., Gong, X.J., Aivazzadeh, S., Tamin, M.N., 2014. R-Curve modelling of mode I delamination in multidirectional carbon/epoxy composite laminates. *Appl. Mech. Mater.* 606, 159–163.
- Wu, M., Wang, W., Song, Z., Liu, B., Feng, C., 2021. Exploring the influence of heterogeneity on hydraulic fracturing based on the combined finite–discrete method. *Eng. Fract. Mech.* 252, 107835.
- Wu, M.Y., Zhang, D.M., Wang, W.S., Li, M.H., Liu, S.M., Lu, J., Gao, H., 2020. Numerical simulation of hydraulic fracturing based on two-dimensional surface fracture morphology reconstruction and combined finite-discrete element method. *J. Nat. Gas Sci. Eng.* 82, 103479.
- Wu, Z., Sun, H., Wong, L.N.Y., 2019. A Cohesive Element-Based Numerical Manifold Method for Hydraulic Fracturing Modelling with Voronoi Grains. *Rock Mech. Rock Eng.* 52, 2335–2359.
- Wu, Z., Xu, X., Liu, Q., Yang, Y., 2018. A zero-thickness cohesive element-based numerical manifold method for rock mechanical behavior with micro-Voronoi grains. *Eng. Anal. Boundary Elem.* 96, 94–108.
- Xiang, J., Munjiza, A., Latham, J.-P., 2009a. Finite strain, finite rotation quadratic tetrahedral element for the combined finite–discrete element method. *Int. J. Numer. Meth. Eng.* 79, 946–978.
- Xiang, J., Munjiza, A., Latham, J.-P., Guises, R., 2009b. On the validation of DEM and FEM/DEM models in 2D and 3D. *Eng. Comput.* 26, 673–687.
- Yan, C., Jiao, Y.-Y., Zheng, H., 2018. A fully coupled three-dimensional hydro-mechanical finite discrete element approach with real porous seepage for simulating 3D hydraulic fracturing. *Comput. Geotech.* 96, 73–89.
- Yan, C., Zheng, H., Sun, G., Ge, X., 2016. Combined finite-discrete element method for simulation of hydraulic fracturing. *Rock Mech. Rock Eng.* 49, 1389–1410.
- Yang, Z.J., Su, X.T., Chen, J.F., Liu, G.H., 2009. Monte Carlo simulation of complex cohesive fracture in random heterogeneous quasi-brittle materials. *Int. J. Solids Struct.* 46, 3222–3234.
- Zhang, F., Dontsov, E., 2018. Modeling hydraulic fracture propagation and proppant transport in a two-layer formation with stress drop. *Eng. Fract. Mech.* 199, 705–720.
- Zhang, F., Dontsov, E., Mack, M., 2017. Fully coupled simulation of a hydraulic fracture interacting with natural fractures with a hybrid discrete-continuum method. *Int. J. Numer. Anal. Meth. Geomech.* 41, 1430–1452.
- Zhelтов, A.K., 1955. 3. Formation of Vertical Fractures by Means of Highly Viscous Liquid, 4th World Petroleum Congress. World Petroleum Congress, Rome, Italy, p. 8.
- Zhuang, L., Kim, K.Y., Diaz, M., Yeom, S., 2020. Evaluation of water saturation effect on mechanical properties and hydraulic fracturing behavior of granite. *Int. J. Rock Mech. Min. Sci.* 130, 104321.